Compressibility effects on the growth and structure of homogeneous turbulent shear flow

By G. A. BLAISDELL[1], N. N. MANSOUR[2]
AND W. C. REYNOLDS[2,3]

[1] School of Aeronautics and Astronautics, Purdue University, West Lafayette, IN 47907, USA

[2] NASA Ames Research Center, Moffett Field, CA 94035, USA

[3] Department of Mechanical Engineering, Stanford University, CA 94305, USA

Compressibility effects within decaying isotropic turbulence and homogeneous turbulent shear flow have been studied using direct numerical simulation. The objective of this work is to increase our understanding of compressible turbulence and to aid the development of turbulence models for compressible flows. The numerical simulations of compressible isotropic turbulence show that compressibility effects are highly dependent on the initial conditions. The shear flow simulations, on the other hand, show that measures of compressibility evolve to become independent of their initial values and are parameterized by the root mean square Mach number. The growth rate of the turbulence in compressible homogeneous shear flow is reduced compared to that in the incompressible case. The reduced growth rate is the result of an increase in the dissipation rate and energy transfer to internal energy by the pressure–dilatation correlation. Examination of the structure of compressible homogeneous shear flow reveals the presence of eddy shocklets, which are important for the increased dissipation rate of compressible turbulence.

1. Introduction

Compressible turbulent flows arise in many important engineering applications, including both conventional gas turbine engines and ramjet propulsion systems, and also in astrophysics (Norman & Winkler 1985). Predictions for these flows require turbulence models. Current models are based primarily on knowledge about incompressible turbulence. A better understanding of compressible turbulence would enable improvement in these models. The objective of this work is to contribute to this new understanding. The work is described in more detail in the report by Blaisdell, Mansour & Reynolds (1991*a*; hereinafter referred to as BMR).

The current work focuses on two simple compressible turbulent flows; (i) the decay of homogeneous isotropic turbulence, and (ii) the build-up of homogeneous turbulence in a uniform mean shear flow. Through study of these simple flows we have learned much about the fine-scale structure of compressible turbulence. In addition, we have determined the relative importance of various terms in the statistical equations, which is key information needed for improved modelling. The turbulent transport terms important for inhomogeneous turbulence are zero in these flows, so comparable information about these terms remains to be found from more complex simulations.

A brief review of important previous contributions to the understanding of compressible turbulence will be useful in discussing the present results. The remainder of this section highlights some relevant past work.

Kovasznay (1953) examined the linearized equations for compressible turbulence and showed the existence of three basic modes – the vorticity mode, the acoustic mode and the entropy mode. The nonlinear interactions of the modes were examined by Chu & Kovasznay (1958) using a perturbation analysis based on small amplitudes. They were able to write down the first-order interaction terms and give estimates as to which ones were important. Their analysis gives some physical insight into compressible turbulence and how the modes affect one another; however, it is not clear how it can be used to study fully nonlinear turbulence for which the decomposition into such modes cannot be made.

A useful decomposition which can be made for finite-amplitude turbulence was provided by Moyal (1951), who introduced a decomposition of the velocity field in Fourier wave space which is the equivalent of Helmholtz's decomposition (see for instance Aris 1962). The velocity is decomposed into a *solenoidal* part, which is divergence free, and a *dilatational* part, which is irrotational. From this decomposition Moyal introduced decomposed velocity spectra. By writing the dynamical equations for the velocity spectrum tensors, he was able to show that, for the case of isotropic turbulence, the two fields interact only through the nonlinear terms.

The two-point statistics and associated spectra of compressible turbulence have been the subject of several theoretical studies. Chandrasekhar (1951) studied two-point correlations of density in compressible isotropic turbulence and derived an integral invariant for density similar to that of Loitsyanskiy for velocity in incompressible turbulence. Considerable theoretical work has been done by Russian researchers on modifications to the Kolmogorov spectrum owing to compressibility (Zakharov & Sagdeev 1970; Kadomtsev & Petviashvili 1973; Moiseev *et al.* 1977; L'vov & Mikhaĭlov 1978*a*, *b*; Moiseev *et al.* 1981). Moiseev *et al.* (1981) find that, for subsonic turbulent Mach numbers, the $-\frac{5}{3}$ slope of the energy spectrum in the inertial subrange is altered by compressibility and a slope of $-(5-M^2)/(3-M^2)$ ensues, so that for Mach numbers of the order of 1 a slope of -2 is obtained.

Other theoretical work of note includes Lighthill's contributions to the foundations of turbulence-generated sound (1952, 1954, 1955, 1956, 1962). Most of this work concerns the radiation of sound to the far field and is not directly applicable to homogeneous turbulence. The nonlinear interaction of shock turbulence in one and two dimensions has been studied by Tatsumi & Tokunaga (1974) and Tokunaga & Tatsumi (1975). Much of the early theoretical research has been summarized and expanded upon by Monin & Yaglom (1971 §§1.7 and 7.20) and by Hinze (1975, §3.9).

Numerical simulations of compressible turbulence have only recently been used as an investigative tool. The first published results of numerical simulations of compressible turbulence were those of Feiereisen *et al.* (1981, 1982). They studied homogeneous shear flow at root mean square (r.m.s.) Mach numbers up to 0.32 using direct numerical simulations with 64^3 grid points. Their simulations did not extend far enough in time to examine the effects of compressibility on the growth of the turbulence; however, they were able to see some effects of compressibility on the structure of the Reynolds stresses and on the pressure–strain terms in the Reynolds stress budgets. Feiereisen *et al.* (1981) also developed a method of generating initial conditions which made the initial flow field nearly incompressible. Such initial conditions have been used subsequently in simulations of decaying isotropic turbulence and have been found to have a strong restraining effect on the development of compressibility effects. However, as is shown in §4 of this paper, compressibility effects in homogeneous shear flow are less dependent on initial conditions than in decaying

isotropic turbulence. Therefore, the type of initial conditions employed by Feiereisen should not have a restraining effect on homogeneous shear flow.

More recent simulations include those of Delorme (1985), who considered homogeneous shear flow using large eddy simulation (LES), and Erlebacher *et al.* (1992), who studied decaying isotropic turbulence for initial r.m.s. Mach numbers up to 0.6 and investigated sub-grid scale models for LES. Most of their simulations used the initial conditions developed by Feiereisen and, therefore, showed little effect of compressibility.

Significant progress in the simulation of compressible turbulence was achieved by Passot & Pouquet (1987). They performed two-dimensional DNS of decaying isotropic turbulence for r.m.s. Mach numbers up to 1.65 using a 256^2 grid. They considered initial conditions that were more general than those used by previous workers. They found that, for r.m.s. Mach numbers below 0.3 and with nearly uniform density initial fields, the density field remained nearly uniform and few compressibility effects were seen. On the other hand, if the initial conditions contained sufficiently strong density and pressure variations, then the flow developed eddy shocklets and compressibility effects became important. At higher r.m.s. Mach numbers, strong eddy shocklets developed regardless of the initial density variation level. Passot, Pouquet & Woodward (1988) later investigated the formation of shocks in decaying isotropic turbulence with initial r.m.s. Mach numbers as high as 4.

Sarkar *et al.* (1991*c*) performed a series of simulations at low r.m.s. Mach number and introduced the idea that compressible turbulence at low Mach numbers tends toward acoustic equilibrium. The behaviour of isotropic turbulence at low r.m.s. Mach numbers was analysed further by Erlebacher *et al.* (1990) and Erlebacher (1990) who developed predictions of how the fraction of energy in the dilatational velocity field and the r.m.s. pressure fluctuations evolve on an acoustic timescale. They also state that a necessary condition for shocks to form at low Mach numbers is that the initial conditions be out of acoustic equilibrium, with large pressure fluctuations present.

Lee, Lele & Moin (1991) studied the existence of eddy shocklets in three-dimensional decaying isotropic turbulence using high-Reynolds-number simulations. They showed that shocklets can arise even when the initial conditions have a purely solenoidal velocity field and do not contain any pressure fluctuations.

Staroselsky *et al.* (1990) studied forced isotropic turbulence and introduced the concept of a scale-dependent effective speed of sound. Dahlburg *et al.* (1990) compared the inverse energy cascade in forced two-dimensional compressible isotropic turbulence with that for the incompressible case.

Kida & Orszag (1990*a, b*) have simulated decaying and forced compressible isotropic turbulence. For the decaying isotropic simulations they do a detailed investigation of the generation of vorticity through the baroclinic torque caused by curved shocks. The forced simulations include purely solenoidal and purely dilatational forcing and show that the two velocity fields are only weakly coupled.

Homogeneous shear flow has been reconsidered only most recently (BMR; Blaisdell, Mansour and Reynolds 1991*b*; Sarkar, Erlebacher & Hussaini 1991*a, b*, 1992). There are several reasons for studying homogeneous shear flow. As mentioned earlier, compressibility effects are less dependent on initial conditions than for isotropic turbulence. The r.m.s. Mach number in homogeneous shear flow increases in time, so compressibility effects become stronger as the flow develops, whereas in decaying isotropic turbulence the r.m.s. Mach number decreases. Also, homogeneous shear flow is a natural extension in complexity over isotropic turbulence.

The results of BMR and Sarkar *et al.* (1991*a*) are generally consistent. One difference

in the studies is that the simulations of BMR include grid sizes up to $192 \times 192 \times 192$, while those of Sarkar *et al.* are at most $128 \times 128 \times 128$. The larger grid allows the simulation to extend further in time. Also, BMR and Sarkar *et al.* investigated different statistics in an effort to characterize compressibility effects. Among other quantities, BMR included the study of the probability density functions of the fluctuations of pressure and density, while Sarkar *et al.* decomposed the pressure into incompressible and compressible parts and studied the evolution of their r.m.s. values. Sarkar *et al.* (1992) considered the structure of the strain rate tensor for compressible turbulence. Lastly, BMR have done a more extensive study of the structure of the turbulence. While there is some overlap in the description of compressibility effects, these two studies provide complementary data.

2. Problem formulation

2.1. *Governing equations*

The time-dependent compressible Navier–Stokes equations are solved assuming that the fluid is a continuum satisfying local thermodynamic equilibrium, the fluid is Newtonian, and that Stokes' relation between the second coefficient of viscosity λ^* and the dynamic viscosity μ^*, $\lambda^* = -\frac{2}{3}\mu^*$, is valid (asterisks denote dimensional quantities). The ideal gas equation of state, $p^* = \rho^* R^* T^*$, is used, where p^* is the pressure, ρ^* the mass density, R^* the specific gas constant, and T^* the temperature. The specific heats are assumed constant, and the simulations use a ratio of specific heats $\gamma = c_p^*/c_v^* = 1.4$. Viscosity obeys a power law temperature dependence, $\mu^*/\mu_0^* = (T^*/T_0^*)^n$. The simulations use $n = 0.67$, the value for nitrogen (White 1974). The Prandtl number, $Pr = \mu^* c_p^*/k^*$, is constant, where k^* is the thermal conductivity, so k^* varies with temperature as μ^*. The simulations use $Pr = 0.7$.

2.1.1. *Non-dimensionalization*

The governing equations are solved in non-dimensional form. We choose as the velocity scale the speed of sound based on the initial mean temperature, $c_0^* = (\gamma R^* T_0^*)^{\frac{1}{2}}$. The non-dimensional velocity is then, $u_i = u_i^*/c_0^*$. For homogeneous turbulence the mean flow field has no intrinsic lengthscale so we use an arbitrary lengthscale, L_0^*, which is related to the computational box size. The non-dimensional spatial coordinate is therefore $x_i = x_i^*/L_0^*$, and time is non-dimensionalized as $t = t^* c_0^*/L_0^*$. The density is scaled on the initial mean density, ρ_0^*, so that $\rho = \rho^*/\rho_0^*$. For consistency the temperature is non-dimensionalized by the initial mean temperature, $T = T^*/T_0^*$. The pressure is non-dimensionalized as $p = p^*/\rho_0^* c_0^{*2}$. The viscosity is non-dimensionalized by the viscosity at the initial mean temperature, $\mu = \mu^*(T^*)/\mu_0^*$ where $\mu_0^* = \mu^*(T_0^*)$. These normalizations leave the ratio of specific heats, γ, the Prandtl number Pr and the Reynolds number $Re = \rho_0^* L_0^* c_0^*/\mu_0^*$ as the only non-dimensional parameters in the governing equations. Note that the Reynolds number is a computational Reynolds number based on the scaling constants.

With the above assumptions and non-dimensionalization, the compressible Navier–Stokes equations can be written as

$$\frac{\partial \rho}{\partial t} + \frac{\partial}{\partial x_i}(\rho u_i) = 0, \qquad (2.1)$$

$$\frac{\partial}{\partial t}(\rho u_j) + \frac{\partial}{\partial x_i}(\rho u_j u_i) = -\frac{\partial}{\partial x_i}\left[p\delta_{ij} - \frac{\mu}{Re}\left(\frac{\partial u_i}{\partial x_j} + \frac{\partial u_j}{\partial x_i} - \frac{2}{3}\frac{\partial u_k}{\partial x_k}\delta_{ij}\right)\right], \qquad (2.2)$$

$$\frac{\partial}{\partial t}(\rho e_T) + \frac{\partial}{\partial x_i}(\rho e_T u_i) = \frac{\partial}{\partial x_i}\left[-p\delta_{ij}u_j + \frac{\mu}{Re}\left(\frac{\partial u_i}{\partial x_j} + \frac{\partial u_j}{\partial x_i} - \frac{2}{3}\frac{\partial u_k}{\partial x_k}\delta_{ij}\right)u_j + \frac{\mu}{(\gamma-1)\,Re\,Pr}\frac{\partial T}{\partial x_i}\right],$$

$$(2.3)$$

where e_T is the non-dimensional total energy per unit mass given by $e_T = e + \frac{1}{2}u_i u_i$ where e is the non-dimensional internal energy per unit mass. The equation of state becomes $p = \rho T/\gamma$.

The convective terms in the momentum equation are recast in a form used originally for incompressible flows by Arakawa (1966) and Kwak, Reynolds & Ferziger (1975) and extended to compressible flows by Feiereisen *et al.* (1981),

$$\frac{\partial}{\partial x_i}(\rho u_j u_i) = \frac{1}{2}u_j\frac{\partial}{\partial x_i}(\rho u_i) + \frac{1}{2}\rho u_i\frac{\partial u_j}{\partial x_i} + \frac{1}{2}\frac{\partial}{\partial x_i}(\rho u_j u_i).$$

$$(2.4)$$

This alternate form of the equations of motion improves the conservation properties of the numerical method, and reduces aliasing errors (BMR).

2.1.2. *Mean flow field*

In performing the direct numerical simulations, the mean velocity field is imposed and a solution is obtained for the fluctuations. There are several types of averages used in discussing compressible turbulence. The Reynolds decomposition involves a mean and a fluctuation,

$$f = \langle f \rangle + f'$$

$$(2.5)$$

where $\langle\ \rangle$ denotes an ensemble average. The Favre (1965 *a*, *b*) mass-weighted average, denoted by a tilde, is defined by

$$\tilde{f} = \langle \rho f \rangle / \langle \rho \rangle.$$

$$(2.6)$$

The *Favre fluctuation*, denoted by f'', is defined by

$$f = \tilde{f} + f''.$$

$$(2.7)$$

By definition $\langle f' \rangle = 0$ and $\overline{\rho f''} = 0$; however, note that $\langle f'' \rangle \neq 0$. By invoking the ergodic hypothesis (see Monin & Yaglom 1971, §§3.3 and 4.7), the ensemble average $\langle f \rangle$, can be replaced by a volume average, which is denoted by f.

In homogeneous turbulence, $\overline{\rho' u_i'} = 0$, from which it follows that Favre averages and Reynolds averages of velocity components are identical, and hence $u_i'' = u_i'$.

The restrictions on the mean fields that allow initially homogeneous turbulence to remain homogeneous have been found by Feiereisen *et al.* (1981), Delorme (1985) and BMR. The mean density field and mean pressure must be uniform in space, $\bar{\rho} = \bar{\rho}(t)$ and $\bar{p} = \bar{p}(t)$. From the equation of state it follows that the mean temperature is uniform in space. It is emphasized that the density, pressure and temperature fluctuations are functions of space and time, $\rho' = \rho'(x, t)$, $p' = p'(x, t)$, and $T' = T'(x, t)$, and only the mean quantities are uniform. For isotropic turbulence the mean velocity is zero, while for homogeneous shear flow the mean velocity has a uniform transverse gradient, which is taken to be in the x_2, or y, direction and is given by $\partial\tilde{u}_1/\partial x_2 = S$, as shown in figure 1.

2.1.3. *Equations in moving coordinates*

The use of periodic boundary conditions is appropriate for homogeneous turbulence, provided that the computational domain is several times larger than the integral scales of the turbulence. However, because the mean velocity field varies in space, which introduces a non-periodic coefficient into the equations, one cannot apply periodic
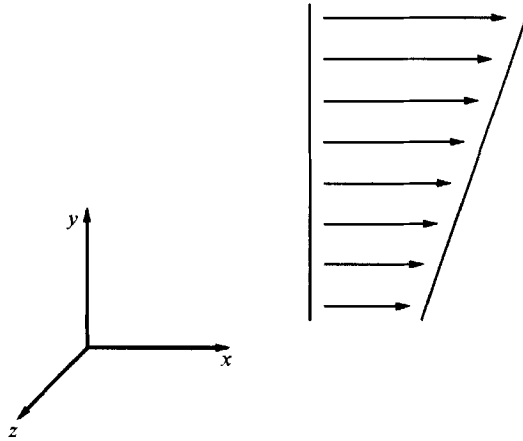
FIGURE 1. Schematic of the mean velocity field for homogeneous turbulent shear flow.

boundary conditions directly. Therefore, we adopt the moving coordinate system first used in numerical simulations by Rogallo (1981),

$$x_i' = B_{ij}(t) x_j \quad (t' = t) \tag{2.8}$$

where initially we have $B_{ij}(0) = \text{diag}(\beta_1, \beta_2, \beta_3)$. We choose

$$\beta_1 = 2\pi/(L_x^*/L_0^*), \beta_2 = 2\pi/(L_y^*/L_0^*) \text{ and } \beta_3 = 2\pi/(L_z^*/L_0^*)$$

so that the computational domain in the new coordinate system is $2\pi \times 2\pi \times 2\pi$. The explicit spatial dependence of the mean velocity field which prevents the use of periodic boundary conditions can be removed if the new coordinate system moves with the mean motion. For the case of shear flow the coordinate transformation matrix is

$$B_{ij}(t) = \begin{pmatrix} \beta_1 & -\beta_1 St & 0 \\ 0 & \beta_2 & 0 \\ 0 & 0 & \beta_3 \end{pmatrix}. \tag{2.9}$$

Solutions for more general cases are given in BMR.

The above transformation does not remove the explicit spatial dependence in the total energy equation because the mean velocity gives rise to a quadratic spatial dependence which cannot be removed by a linear transformation. However, we can use the mean momentum equation to eliminate the quadratic spatial dependence, obtaining an equation for what we refer to as the 'pseudo total energy',

$$\phi = \rho e + \tfrac{1}{2}\rho u_i'' u_i''. \tag{2.10}$$

The pseudo total energy is the total energy without the contribution from the mean velocity. An alternative is to use a pressure equation as was done by Feiereisen et al. (1981). The advantage of using the equation for ϕ instead of that for pressure is that the evaluation of three fewer derivatives is required making the use of the ϕ equation somewhat less computationally expensive. Also, for the isotropic case, ϕ is the same as the total energy.

The equations of motion for the case of shear flow, including the modified convective terms, are summarized below:

$$\frac{\partial \rho}{\partial t'} = -\frac{\partial}{\partial x_k'}(\rho u_i'' B_{ki}), \tag{2.11}$$

$$\frac{\partial}{\partial t'}(\rho u_j'') = -\rho u_2'' S \delta_{j1} - \tfrac{1}{2} u_j'' \frac{\partial}{\partial x_k'}(\rho u_i'' B_{ki}) - \tfrac{1}{2}(\rho u_i'' B_{ki})\frac{\partial u_j''}{\partial x_k'}$$

$$+\frac{\partial}{\partial x_k'}[B_{ki}(\sigma_{ji} - \tfrac{1}{2}\rho u_j'' u_i'')], \tag{2.12}$$

$$\frac{\partial \phi}{\partial t'} = S(\sigma_{12} - \rho u_1'' u_2'') + \frac{\partial}{\partial x_k'}\left[B_{ki}\left((\sigma_{ij} - \phi\delta_{ij})u_j'' + \frac{\mu}{(\gamma-1)\,Re\,Pr}\frac{\partial T}{\partial x_j'}B_{ji}\right)\right], \tag{2.13}$$

where
$$\sigma_{ij} = -p\delta_{ij} + \frac{\mu}{Re}\left(\frac{\partial u_i''}{\partial x_k'}B_{kj} + \frac{\partial u_j''}{\partial x_k'}B_{ki} - \tfrac{2}{3}d'\delta_{ij} + S\delta_{i1}\delta_{j2} + S\delta_{i2}\delta_{j1}\right), \tag{2.14}$$

$$d' = \frac{\partial u_i''}{\partial x_j'}B_{ji}. \tag{2.15}$$

A formulation of the equations of motion for more general mean flows is given in BMR.

2.2. *Numerical method*

2.2.1. *Choice of numerical method*

For turbulent flows the most outstanding requirement imposed on the numerical method is the wide range of lengthscales that need to be represented accurately. For this reason spectral methods are commonly used for direct simulations of incompressible turbulence. For simulations of compressible turbulence, however, the use of spectral methods causes some concern. In compressible turbulence, shock waves may form, and it is well known that spectral methods lose their characteristic exponential convergence when the solution contains steep gradients.

Passot & Pouquet (1987) successfully used a spectral method to study two-dimensional compressible decaying isotropic turbulence. They showed that simulations can be performed with a spectral method at fairly high r.m.s. Mach numbers as long as the Reynolds number is sufficiently low. Since the simulations are for viscous flows, any shock waves which develop will have a finite thickness. As long as they are adequately resolved a spectral method will produce an accurate solution. We shall see from the simulation results that weak to moderately strong shocks do form in the turbulence and that they cause some resolution problems. The issue of resolution is discussed further in §§4.5 and 5.3.

2.2.2. *Spatial differencing*

The method implemented is a pseudo-spectral Fourier method in which the nonlinear terms are formed in physical space. The transformations between physical space and Fourier wave space are implemented using a fast Fourier transform (FFT) algorithm.

Nonlinear terms lead to the formation of Fourier modes which do not lie within the resolved range of wavenumbers, which for each dimension is given by $k_n = 2\pi n/L$ with $n = -\tfrac{1}{2}N+1, \ldots, \tfrac{1}{2}N$. When such modes are discretized they mimic (or are 'aliased' to) modes which are within the resolved wavenumber range. This gives rise to 'aliasing' errors. (For a good discussion of aliasing errors see Rogallo 1981.) In the current work, aliasing errors are controlled in two ways. In §2.1 the equations of motion were written with a modified form of the convective terms. BMR have shown the modified convective terms reduce the magnitude of aliasing errors. The second means of controlling aliasing errors is to ensure that the simulations are well resolved, so that the magnitude of the unresolved Fourier modes which are formed from nonlinear terms

will be small and thus the aliasing errors will be small. Aliasing errors also arise during the remeshing procedure for shear flow, discussed in §2.2.4, and these are explicitly removed.

2.2.3. *Time advancement*

The time advancement scheme used in this study is a third-order compact storage Runge–Kutta method developed by Wray (1986). One has a choice of advancing the Fourier coefficients or local physical variables, and for computational economy we chose to advance the local variables. With this choice, the formation of nonlinear terms does not require any Fourier transforms; however, transforms are needed to evaluate derivatives. For the governing equations there are fewer derivatives that need to be evaluated than nonlinear terms. Thus the number of FFTs required is less if time advancement is performed in physical space. This is the method chosen for the current work.

2.2.4. *Remeshing*

During a simulation of shear flow the computational domain deforms with the mean velocity, and the grid, which is initially Cartesian, becomes highly skewed at later times. In order to avoid a highly skewed mesh, the periodic extension of the flow field is used to interpolate the data onto a coordinates system skewed in the opposite sense. The grid then advances back toward a Cartesian mesh. This process is depicted in figure 2. The remeshing process takes place at multiples of the remesh time, t_R, which is given by

$$t_R = (\beta_2/\beta_1)/2S. \qquad (2.16)$$

Most of the shear flow simulations use domains with $\beta_1 = 0.5$ and $\beta_2 = 1.0$ so that $L_x = 2L_y$ and $t_R = 1/S$.

A straightforward approach to the remeshing process leads to aliasing errors. In the current approach, we follow Delorme (1985) and avoid aliasing errors by carrying out the remesh in wave space. The modes which do not lie within the resolved wavenumber range for the new grid are simply discarded. The Fourier coefficients for the modes in the new system which do not correspond to modes from the old systems are set to zero.

2.3. *Initial conditions*

To begin the simulations, initial conditions for the dependent variables must be provided. All of the simulations performed began with isotropic initial conditions. The fluctuations of each quantity are parameterized by an r.m.s. fluctuation level and the shape of the three-dimensional correlation spectrum. The initial fluctuations are specified as random fields following a procedure developed by Rogallo (1981). Details are given in BMR.

For compressible turbulence there are more parameters that need to be specified than for incompressible turbulence. When non-dimensionalizing the problem, the density is scaled by its initial mean value. Therefore, the mean non-dimensional density is unity. However, the r.m.s. level of the density fluctuations must be specified along with the shape of the density variance spectrum. In contrast to the incompressible case, the velocity field for compressible turbulence does have an intrinsic velocity scale – the initial mean speed of sound. Thus, in specifying the non-dimensional problem, the initial r.m.s. velocity must be given, whereas for the incompressible case the velocity can be scaled so that the r.m.s. velocity is unity. Since the velocity is non-dimensionalized by the speed of sound based on the initial mean temperature, the non-dimensional r.m.s. velocity is similar to the r.m.s. Mach number. Furthermore, the velocity can be decomposed into solenoidal and dilatational components, $u_i^{s'}$ and $u_i^{d'}$,
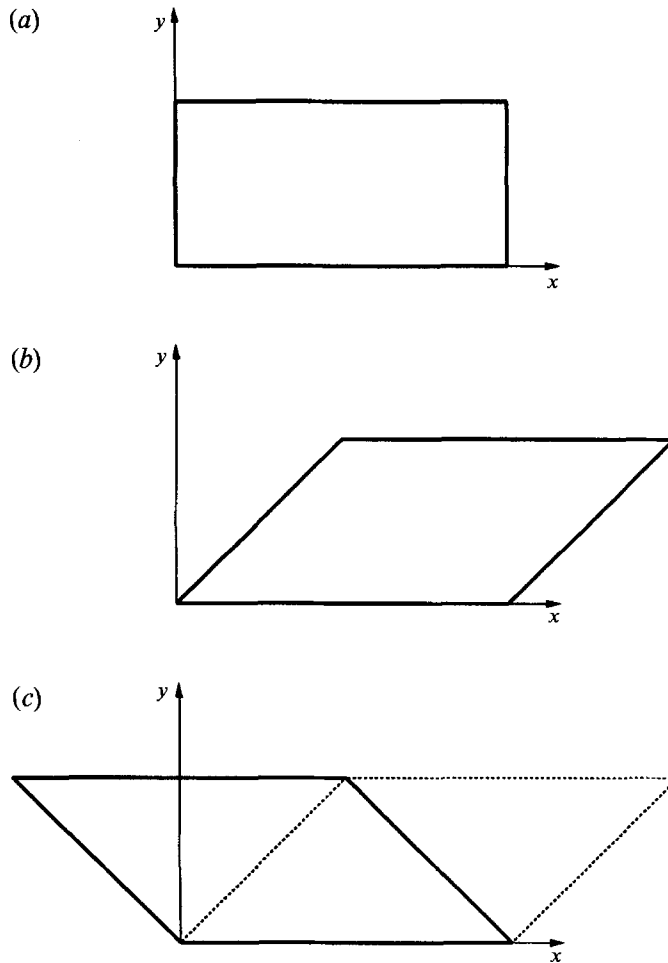
(a)

(b)

(c)

FIGURE 2. Computational domain for shear flow when (a) the grid is Cartesian,
(b) just before remeshing, (c) just after remeshing.

respectively, using Helmholtz' decomposition. The relative r.m.s. levels of these two velocity fields is parameterized by

$$\chi = \overline{u_i^{d''} u_i^{d''}}/(\overline{u_j^{d''} u_j^{d''}} + \overline{u_j^{s''} u_j^{s''}}) = \overline{u_i^{d''} u_i^{d''}}/\overline{u_j'' u_j''}. \tag{2.17}$$

Also, separate velocity correlation spectra, $E^s(k)$ and $E^d(k)$, may be used. The temperature fluctuations are also specified; alternatively, the pressure fluctuations could be given. The temperature is scaled on its initial mean value and thus its initial mean value is unity. One needs to specify the initial r.m.s. fluctuation level of the temperature and the temperature variance spectrum.

The specification of initial conditions for compressible turbulence introduces many parameters. In order to make the problem tractable some simplifications are made. We use the same spectrum shape for all the fluctuating fields. Thus

$$E_\rho(k) \propto E^s(k) \propto E^d(k) \propto E_T(k) \propto E(k). \tag{2.18}$$

Although the spectrum shapes are the same the r.m.s. values of the variables can differ. Most of the simulations make use of a box-type spectrum shape for which $E(k)$ is constant in a certain wavenumber band and zero outside. This was done in order to

compare to the incompressible simulations of Rogers, Moin & Reynolds (1986). An alternate spectrum shape is used for some of the isotropic simulations and is described in §3.3.

2.4. *Test cases*

The computer program developed for this work was tested using two types of test problem. The first includes the shock tube problem of Passot & Pouquet (1987) and some extensions. This problem tests the programming of the equations of motion without having an imposed mean velocity field. The second set of tests involves laminar flow with an imposed mean velocity field and tests the programming of the mean velocity.

The results of these tests help give confidence that the equations of motion are programmed correctly. Details of the tests run and their results are given in BMR.

3. Decaying isotropic turbulence

The simplest kind of turbulence is isotropic and, therefore, isotropic turbulence forms a natural starting point for the study of compressible turbulence. This flow has been considered in many recent investigations. The simulations presented in this section are limited in scope, but they show an important aspect of decaying isotropic compressible turbulence which is later contrasted to the behaviour of homogeneous shear flow. It is shown that compressibility effects in decaying isotropic turbulence are highly dependent on initial conditions. This effect makes it difficult to model compressible isotropic turbulence and implies that, in general, simple algebraic turbulence models cannot capture compressibility effects for decaying isotropic turbulence. The shear flow simulations presented in the next section are found to be less dependent on initial conditions, so that compressibility effects are more easily parameterized. In both cases, the observed behaviour can be understood from linear theory.

3.1. *Linear theory for compressible isotropic turbulence*

Examination of the linear equations of motion, pioneered by Kovasznay (1953), gives insight into the physics of compressible turbulence. He showed that compressible turbulence consists of three modes which act independently. A linear analysis similar to that of Kovasznay is provided below in order that the results for isotropic turbulence may be contrasted with those for shear flow, discussed in §4.

The inviscid case is examined first. Consider the equations of motion with the mean velocity set to zero and the molecular diffusion terms neglected. Assume that the fluctuations of density, pressure and temperature are small with respect to their mean values. Also, assume that the magnitude of the velocity is small (since the velocity is non-dimensionalized by the speed of sound based on the initial mean temperature, this is the same as assuming a low r.m.s. Mach number). Using the above assumptions and keeping only linear terms, one obtains the inviscid linearized equations. From these linearized equations one can derive equations for the vorticity, pressure and entropy. These are

$$\frac{\partial \omega_i'}{\partial t} = 0, \tag{3.1}$$

$$\frac{\partial^2 p'}{\partial t^2} - \bar{c}^2 \frac{\partial^2 p'}{\partial x_j \partial x_j} = 0, \tag{3.2}$$

$$\frac{\partial s'}{\partial t} = 0, \tag{3.3}$$

where ω_i' is the fluctuating vorticity, $\bar{c}$ is the mean speed of sound, and s' is the fluctuating entropy.

Equations (3.1), (3.2) and (3.3) show that the fields of vorticity, pressure and entropy are independent of one another. These fields are called 'modes' in the classical literature on compressible turbulence (Kovasznay 1953; Morkovin 1962), and the three fields are referred to as the vorticity mode, the acoustic mode and the entropy mode. Equation (3.1) shows that the vorticity field is frozen. From (3.2) we see that the pressure fluctuations obey a wave equation. Finally, the entropy field is also frozen, as displayed by (3.3). Notice that for turbulence with no mean velocity gradients the three modes are decoupled. This is an important point to which we will return.

If one accounts for viscosity in the linearized analysis, a diffusion equation is obtained for the vorticity,

$$\frac{\partial \omega_i'}{\partial t} = \frac{\bar{\mu}}{\bar{\rho} \, Re} \frac{\partial^2 \omega_i'}{\partial x_j \partial x_j}. \tag{3.4}$$

The vorticity field remains independent of the pressure and entropy. However, the pressure and entropy fields become coupled.

Kovasznay was able to obtain three independent modes for the viscous case by splitting the entropy field into two parts, one of which is associated with the pressure fluctuations, or the acoustic mode. By doing this, the modes no longer consists of single fields; the acoustic mode has a pressure field and an entropy field associated with it. The equations for these two fields are coupled to each other, but they are independent of the vorticity and the other part of the entropy. The viscous analysis of Kovasznay assumed $Pr = \frac{3}{4}$. For other values of the Prandtl number it is necessary to split both the pressure and the entropy into two parts in order to obtain three independent modes. The concept of independent modes seems to become clouded when it is necessary to split physical fields, such as the pressure and entropy, into different parts. Yet, for the inviscid linear case the decomposition is clear, and for the viscous case one can see that the vorticity is independent of the pressure and entropy.

Chu & Kovasznay (1958) developed a nonlinear theory which evaluates the interactions of the modes. While the decomposition of the turbulence into modes is a useful concept for understanding the physics of compressible turbulence, a general turbulent flow field cannot be decomposed into independent modes. The theories based on the linearization of the equations of motion give qualitative information, but they cannot be used to analyse the simulation results in a quantitative manner.

In this work we will refer to modes with the understanding that they are not defined in any concrete sense for a fully nonlinear turbulent flow field. We will loosely associate the vorticity and solenoidal velocity fields with the vorticity mode; the pressure, density and dilatational velocity fluctuations with the acoustic mode; the entropy field with the entropy mode.

3.2. *Isotropic simulations*

Simulations of decaying isotropic turbulence were performed with initial r.m.s. Mach numbers from 0.3 to 0.7. For the purposes of modelling, it was hoped that measures of compressibility could be expressed as functions of the turbulent Mach number. Initial condition parameters other than the r.m.s. Mach number were also varied to see their effect.

The parameters for the simulations discussed below are given in table 1. Each simulation used a 96^3 grid. M_0 in table 1 is the initial non-dimensional velocity variance, which is a close approximation to the r.m.s. Mach number. It should be pointed out that the value of M_0 given in table 1 is the initial value and that the instantaneous r.m.s.

Case	idc96	ie96	ifd96	ife96	ikgc96	ikhb96
$E_0(k)^\dagger$	1	1	1	1	2	2
$(\overline{\rho'\rho'})_0^{\frac{1}{2}}$	0.0	0.15	0.15	0.0	0.0	0.15
$(\overline{T'T'})_0^{\frac{1}{2}}$	0.0	0.15	0.15	0.0	0.0	0.15
χ_0	0.0	0.25	0.25	0.0	0.0	0.1
M_0	0.3	0.3	0.7	0.7	0.5	0.5
Re	515	536	172	166	‡	‡
Re_{T_0}	160.8	160.9	90.2	91.0	500	500
t_{final}/τ_0	4.9	5.0	4.9	4.6	2.0	2.0

† Type of initial spectrum: (1) top hat spectrum with energy in the wavenumber band $8 \leqslant k \leqslant 16$, (2) $E(k) \sim k^4 e^{-2(k/k_0)^2}$ with $k_0 = 6$.
‡ Computational Reynolds number adjusted to keep Re_T constant until $t = \tau_0$.

TABLE 1. Initial condition and run parameters for the isotropic simulations

Mach number, $M_{r.m.s.}$, quickly decays to lower values. For each Mach number, two types of initial condition were used. The first was an attempt to include fluctuations only from the vorticity mode. For this type, the initial density, pressure and temperature fields were uniform and the velocity fluctuations were purely solenoidal. The second kind of initial condition imposed allowed for some fluctuations in the acoustic and entropy modes. These simulations were used to investigate the effects of the initial r.m.s. Mach number and the effects of initial acoustic and entropic fluctuations. The results of the simulations are discussed below in the context of evaluating turbulence models.

3.3. Dependence of compressibility effects on initial conditions

Sarkar *et al.* (1991 c) and Zeman (1990) have proposed models for the effects of compressibility on the dissipation rate of the turbulent kinetic energy. These models are formulated in terms of algebraic relations involving the r.m.s. Mach number. In this section we show that for isotropic turbulence compressibility effects on the dissipation rate depend more on the initial conditions than on the r.m.s. Mach number. Therefore, in general, these models cannot work for isotropic turbulence.

The dissipation rate of turbulent kinetic energy is well approximated by

$$\epsilon = \underbrace{\frac{\tilde{\mu}}{Re}\overline{\omega_i'\omega_i'}}_{\epsilon_s} + \underbrace{\frac{4}{3}\frac{\tilde{\mu}}{Re}\overline{\frac{\partial u_i''}{\partial x_i}\frac{\partial u_j''}{\partial x_j}}}_{\epsilon_d}, \qquad (3.5)$$

where ϵ_s is the solenoidal dissipation rate and ϵ_d is the dilatational dissipation rate. The full expression for ϵ has an additional term involving fluctuations of viscosity; however, it has been found from the simulations to be negligible. The dissipation rate can be written as

$$\epsilon = \epsilon_s + \epsilon_d = \epsilon_s(1 + \epsilon_d/\epsilon_s). \qquad (3.6)$$

Sarkar *et al.* (1991 c) and Zeman (1990) have proposed using an incompressible turbulence model to determine ϵ_s and incorporating compressibility effects through ϵ_d/ϵ_s. Both models are formulated as $\epsilon_d/\epsilon_s = f(M_T)$. (The turbulent Mach number, M_T, as defined by Sarkar *et al.* and Zeman is very close in value to the r.m.s. Mach number and, therefore, little distinction is made here between the two.)
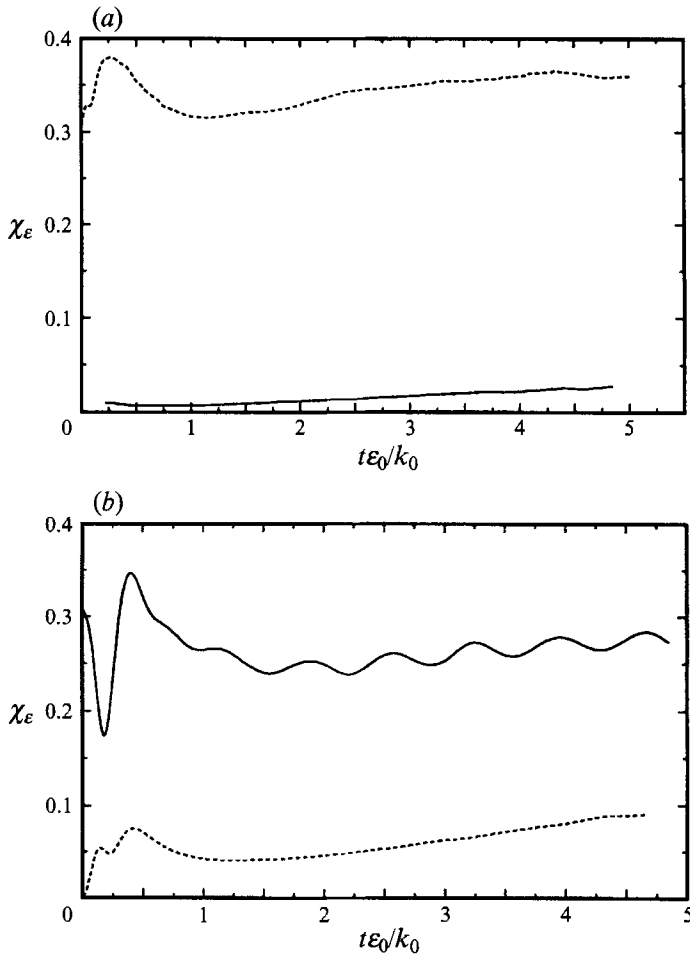
FIGURE 3. Evolution of χ_ϵ for (a) simulations ———, idc96 and ————, ie96 which have $M_0 = 0.3$ and (b) simulations ———, ifd96 and ————, ife96 which have $M_0 = 0.7$.

A measure of compressibility is the fraction of the dissipation rate due to dilatation,

$$\chi_\epsilon = \frac{\epsilon_d}{\epsilon_s + \epsilon_d} = \frac{\epsilon_d/\epsilon_s}{1 + \epsilon_d/\epsilon_s}. \tag{3.7}$$

Figure 3(a) shows the history of χ_ϵ for simulations idc96 and ie96, both of which have an initial r.m.s. Mach number of 0.3 but differ in their initial value of χ and hence χ_ϵ. The value of χ_ϵ is seen to remain very different for the two simulations. The runs extend to five initial eddy turnover times, which is a significant amount of time. Therefore, this result is not expected to change by merely continuing the simulations further. The same plot is given in figure 3(b) for simulations ifd96 and ife96, which both have an initial r.m.s. Mach number of 0.7. As with the other two simulations, χ_ϵ remains different. From these comparisons we see that the development of χ_ϵ in isotropic turbulence is highly dependent on its initial value and cannot be parameterized solely by the turbulent Mach number.

The behaviour of χ_ϵ for the decaying isotropic simulations is consistent with the linear theory discussed in §3.1. From the inviscid linearized equations we saw that the
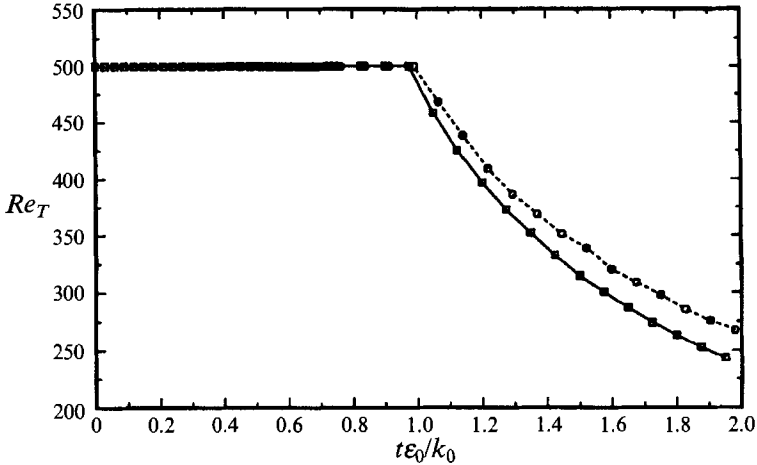
FIGURE 4. History of Re_T for ——, ikgc96 and ----, ikhb96.

vorticity, pressure and entropy fields in compressible turbulence are decoupled. With the addition of viscosity the entropy and pressure fields become coupled, but they still are not coupled to the vorticity field. Any interaction between the vorticity and the pressure and entropy fields is a result of nonlinearities. The weak nonlinear coupling of the modes gives rise to the strong dependence of the turbulence on the initial amplitudes of the various fields. Because the vorticity mode is decoupled, its strength depends mainly on the initial level of the vorticity fluctuations.

Erlebacher (1990) has also shown that compressibility effects in isotropic turbulence are dependent on initial conditions. Erlebacher *et al.* (1990) have used ideas from linear acoustics to predict the evolution of χ_ϵ over an acoustic timescale (assumed to be much smaller than the timescale for viscous decay). Their predictions are based on the pressure and dilatational velocity fluctuations coming to an equilibrium. The predicted levels of χ_ϵ agree well with their simulation results showing that linear theory does give insight into the behaviour of compressible turbulence.

Both the simulations discussed above and those of Erlebacher *et al.* (1990) were carried out at low Reynolds numbers. The initial values of the turbulent Reynolds number, $Re_T = \bar{\rho}^{*2}q^{*4}/\epsilon^*\tilde{\mu}^*$, for the current simulations are given in table 1. Since nonlinear vortex interactions are weak for low-Reynolds-number turbulence, there was some concern that the observed dependence on initial conditions was merely due to the low Reynolds numbers of the simulations.

In order to test whether the dependence on initial conditions would persist at higher Reynolds numbers, simulations ikgc96 and ikhb96 were performed. As shown in table 1, the initial conditions for the two simulations are the same except that ikgc96 contains no energy in the dilatational velocity field and no density or temperature fluctuations while ikhb96 contains significant acoustic disturbances. The initial turbulent Reynolds number for both simulations is $Re_T = 500$ which is significantly higher than that of the simulations discussed above. The initial spectrum was modified to the form

$$E(k) \propto k^4 \exp\left[-2(k/k_0)^2\right], \tag{3.8}$$

where the spectrum peak is located at k_0. This spectrum shape is closer to that of developed turbulence than the box-type spectrum used in the other simulations described in table 1. More importantly, k_0 was chosen to be 6; by moving the peak in the spectrum to lower wave numbers, we were able to simulate turbulence at higher
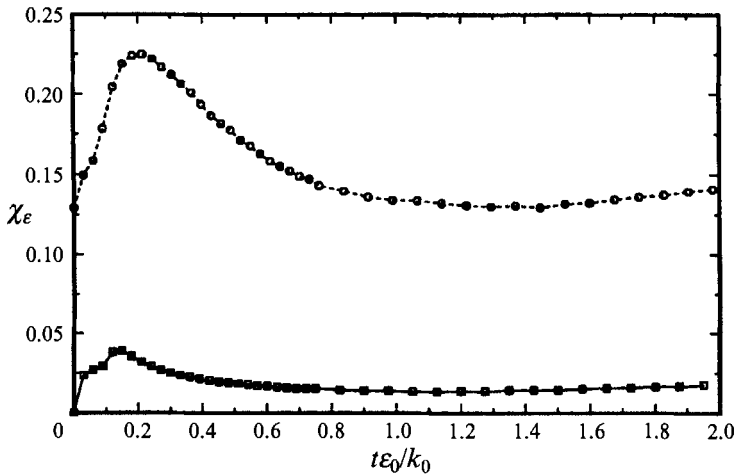
FIGURE 5. Evolution of χ_ε for ——, ikgc96 and - - - -, ikhb96.

Reynolds numbers. However, this also means that, as the lengthscales of the turbulence grow, the effects of the periodic boundary conditions are felt sooner.

The Reynolds numbers of the previous simulations quickly decay during the early part of the simulation. Since it takes some time for a simulation to develop realistic turbulence, we were concerned that Re_T would have decayed to too low a value by the time the simulations were useful. Therefore, it was decided to adjust the computational Reynolds number during the first part of the simulation so that Re_T remained constant. This was done for a period of one initial eddy turnover time, after which time the computational Reynolds number was held fixed and Re_T was allowed to decay. In this way developed turbulence at high Reynolds numbers is obtained. Although the Reynolds number remains high, the r.m.s. Mach number decays during the entire course of the simulations. The history of Re_T for the two simulations is shown in figure 4. After Re_T is released it decays to about 250 which is still significantly large, and so the results should not be clouded by low-Reynolds-number effects.

The evolution of χ_ε for the two simulations is given in figure 5. Both simulations show a large increase at early times followed by decay and then a slight increase. The value of χ_ε for simulation ikhb96 remains much greater than that for ikgc96. This is true during the time when Re_T is held fixed and after it is released. Therefore, it appears that the development of χ_ε is dependent upon initial conditions even at higher Reynolds numbers.

The acoustic fluctuations become very strong in these two simulations, especially for ikhb96, suggesting the formation of shock waves. Examination of the flow fields shows shock-like structures; however, they are not well resolved. Because of the resolution issue, the evidence that χ_ε depends upon initial conditions even at high Reynolds numbers is not conclusive, but we believe this to be the case.

The dependence of χ_ε on initial conditions also holds for other measures of compressibility, such as χ and the variances of density and pressure. This dependence on initial conditions means that simple algebraic turbulence models such as those of Sarkar *et al.* (1991*c*) and Zeman (1990) will not work for decaying isotropic turbulence. For very high r.m.s. Mach numbers the interactions between the vorticity and the acoustic modes may be strong enough that χ_ε might become independent of its initial value. However, this would require r.m.s. Mach numbers much higher than those

simulated here. We will see in the next section that compressible homogeneous shear flow is less dependent on initial conditions than isotropic turbulence and, therefore, compressibility effects are more easily parameterized.

4. Compressible homogeneous turbulent shear flow

Homogeneous shear flow is the primary focus of this study. Turbulent shear flow presents an additional level of complexity, compared to isotropic turbulence, because of the anisotropy of the flow. The shear flow simulations performed, and the subsequent results, are discussed in this section. We begin by examining the linear equations of motion to gain some physical insight into compressible homogeneous shear flow. While compressibility effects in the decaying isotropic simulations presented in the previous section are dependent on initial conditions, it is found that, for homogeneous shear flow, measures of compressibility evolve to become independent of their initial values and are parameterized by the instantaneous r.m.s. Mach number. This property makes compressible turbulent shear flow more straightforward to model than isotropic turbulence. Some recently proposed modifications to k–ϵ models are examined.

4.1. *Linear theory for compressible turbulent shear flow*

Just as examination of the linearized equations of motion for decaying isotropic turbulence in the previous section proved useful, the linear analysis gives insight into the physics of compressible homogeneous turbulent shear flow. The vorticity and acoustic modes, which are decoupled for the isotropic case, become coupled in the presence of mean shear. The importance of this direct coupling to the independence from initial conditions of compressibility effects is discussed in §4.3.

The inviscid linearized equations are derived from the equations of motion in the transformed coordinate system, (2.11)–(2.13), with the viscous and heat conduction terms neglected. From the linearized equations one can derive the equations for the vorticity, dilatation, pressure and entropy fluctuations, which are

$$\frac{\partial \omega_1'}{\partial t'} = \tfrac{1}{2} S \omega_2' - S s_{13}', \tag{4.1}$$

$$\frac{\partial \omega_2'}{\partial t'} = \tfrac{1}{2} S \omega_1' - S s_{23}', \tag{4.2}$$

$$\frac{\partial \omega_3'}{\partial t'} = S d' - S s_{33}', \tag{4.3}$$

$$\frac{\partial d'}{\partial t'} = -S \omega_3' - 2 S s_{12}' - \frac{1}{\bar{\rho}} \frac{\partial^2 p'}{\partial x_l' \partial x_m'} B_{ll} B_{mi}, \tag{4.4}$$

$$\frac{\partial p'}{\partial t'} = -\gamma \bar{p} d', \tag{4.5}$$

$$\frac{\partial s'}{\partial t'} = \frac{\partial s'}{\partial t} + \tilde{u}_i \frac{\partial s'}{\partial x_i} = 0, \tag{4.6}$$

where

$$s_{ij}' = \frac{1}{2} \left(\frac{\partial u_i''}{\partial x_k'} B_{kj} + \frac{\partial u_j''}{\partial x_k'} B_{ki} \right) \tag{4.7}$$

is the fluctuating strain rate tensor, and d' is the fluctuating divergence of the velocity given by (2.15). The equations for the pressure and dilatation can be combined to

obtain a wave-type equation; however, for the current purpose, it is not useful to do so. The mean shear couples the dilatation with the vorticity and the fluctuating strain rate. This coupling is more clearly seen by examining the Fourier transforms of the linearized equations.

The Fourier coefficients (denoted by $\frown$) of the velocity can be written in terms of the vorticity and the dilatation as

$$\hat{u}_p'' = i\frac{\epsilon_{pqj}k_r'B_{rq}\hat{\omega}_j'}{k_m'B_{ml}k_n'B_{nl}} - i\frac{k_j'B_{jp}\hat{d}'}{k_m'B_{ml}k_n'B_{nl}}, \tag{4.8}$$

where ϵ_{pqj} is the alternating tensor. The strain rate in Fourier wave space is given by

$$\hat{s}_{jl}'' = \tfrac{1}{2}i(k_p'B_{pl}\hat{u}_j'' + k_p'B_{pj}\hat{u}_l''). \tag{4.9}$$

Substituting (4.8) into (4.9) and using this relation for the strain rate, the vorticity, dilatation and pressure equations in Fourier space are

$$\frac{\partial\hat{\omega}_1'}{\partial t'} = \tfrac{1}{2}S\hat{\omega}_2' - \frac{S}{k_a'B_{ac}k_b'B_{bc}}(\tfrac{1}{2}k_1'B_{11}(k_2'B_{22}+k_1'B_{12})\,\hat{\omega}_1'$$
$$-\tfrac{1}{2}((k_1'B_{11})^2-(k_3'B_{33})^2)\,\hat{\omega}_2'$$
$$-\tfrac{1}{2}(k_2'B_{22}+k_1'B_{12})\,k_3B_{33}\,\hat{\omega}_3'+k_1'B_{11}k_3'B_{33}\,\hat{d}'), \tag{4.10}$$

$$\frac{\partial\hat{\omega}_2'}{\partial t'} = \tfrac{1}{2}S\hat{\omega}_1' - \frac{S}{k_a'B_{ac}k_b'B_{bc}}(\tfrac{1}{2}((k_2'B_{22}+k_1'B_{12})^2-(k_3'B_{33})^2)\,\hat{\omega}_1'$$
$$-\tfrac{1}{2}k_1'B_{11}(k_2'B_{22}+k_1'B_{12})\,\hat{\omega}_2'$$
$$+\tfrac{1}{2}k_1'B_{11}k_3'B_{33}\,\hat{\omega}_3'+(k_2'B_{22}+k_1'B_{12})\,k_3'B_{33}\,\hat{d}'), \tag{4.11}$$

$$\frac{\partial\hat{\omega}_3'}{\partial t'} = \frac{-S}{k_a'B_{ac}k_b'B_{bc}}((k_2'B_{22}+k_1'B_{12})\,k_3'B_{33}\,\hat{\omega}_1'-k_1'B_{11}k_3'B_{33}\,\hat{\omega}_2'$$
$$+(k_3'B_{33})^2\,\hat{d}')+S\hat{d}', \tag{4.12}$$

$$\frac{\partial\hat{d}'}{\partial t'} = -\frac{2k_1B_{11}S}{k_a'B_{ac}k_b'B_{bc}}((k_2'B_{22}+k_1'B_{12})\,\hat{d}'-k_3'B_{33}\,\hat{\omega}_1'+k_1'B_{11}\,\hat{\omega}_3')$$
$$+\frac{k_a'B_{ac}k_b'B_{bc}}{\bar{\rho}}\hat{p}', \tag{4.13}$$

$$\frac{\partial\hat{p}'}{\partial t'} = -\gamma\bar{p}\hat{d}'. \tag{4.14}$$

Here we clearly see that for compressible homogeneous shear flow the vorticity mode and the acoustic mode are coupled. The dilatation appears on the right-hand side of the vorticity equations, and the vorticity appears on the right-hand side of the dilatation equation. This direct coupling results in the shear flow being less dependent on initial conditions than decaying isotropic turbulence as is shown in §4.3.

4.2. *Compressible shear flow simulations*

The parameters governing compressible homogeneous shear flow are the same as those for compressible decaying isotropic turbulence with the addition of the shear rate, $S^* = \partial\tilde{u}_1^*/\partial x_2^*$. The shear rate is non-dimensionalized by c_0^* and L_0^* giving $S = \partial\tilde{u}_1/\partial x_2$. A physically meaningful non-dimensional shear rate is formed from the turbulence velocity scale, q^*, where $q^{*2} = \overline{\rho^*u_i''^*u_i''^*}/\bar{\rho}^*$, and a lengthscale, l^*. Choosing the large eddy lengthscale, $l^* = \bar{\rho}^*q^{*3}/\epsilon^*$, gives

$$S^* = \bar{\rho}^*S^*q^{*2}/\epsilon^* = \bar{\rho}Sq^2/\epsilon. \tag{4.15}$$

Case	sia96	sic96	scb96/192	scc96‡	scd96	sha192
$E_0(k)$†	1	1	1	1	1	2
$(\overline{\rho'\rho'})^{\frac{1}{2}}_0$	0.0	0.04	0.0	0.0	0.15	0.0
$(\overline{T'T'})^{\frac{1}{2}}_0$	0.0	0.016	0.0	0.0	0.15	0.0
χ_0	0.0	0.043	0.0	0.0	0.25	0.0
M_0	0.2	0.2	0.3	0.3	0.3	0.4
S	1.02	1.03	1.53	1.53	1.59	4.08
Re	864	870	576	576	600	864
St_{final}	8	8	14	14.14	14	24

Case	sea96	sed96	see96	sef128	seg96§
$E_0(k)$†	1	1	1	1	1
$(\overline{\rho'\rho'})^{\frac{1}{2}}_0$	0.0	0.05	0.0	0.0	0.0
$(\overline{T'T'})^{\frac{1}{2}}_0$	0.0	0.05	0.0	0.0	0.0
χ_0	0.0	0.05	0.10	0.25	0.0
M_0	0.5	0.5	0.5	0.5	0.5
S	2.55	2.57	2.59	2.65	2.55
Re	346	349	351	360	346
St_{final}	16	14	14	14	14

† Type of initial spectrum: top hat spectrum with energy in the wave number band (1) $8 \leqslant k \leqslant 16$, (2) $16 \leqslant k \leqslant 32$.

‡ Same as scb96 except $\beta_1 = 0.5$, $\beta_2 = 1/\sqrt{2}$, $\beta_3 = 1.0$ to test the effects of the domain size in the x_2-direction.

§ Same as sea96 except the initial conditions were produced with a different seed for the random number generator.

TABLE 2. Initial condition and run parameters for the shear flow simulations

The above choice for the lengthscale l^* is not unique, but it has been the usual choice in previous studies of homogeneous shear flow.

Table 2 lists the parameters for the shear flow simulations performed. All of the runs had a initial non-dimensional shear rate, $S^* = 5.9$, and an initial turbulent Reynolds number, $Re_T = 200$. The initial r.m.s. Mach number and other initial compressibility parameters were varied. Most of the runs used a 96^3 grid; run sha192 used a 192^3 grid with a larger computational domain, and simulation scb192 is a 192^3 refinement of scb96 which goes from $St = 10$ to $St = 12$. The purpose of these simulations is to investigate the effect of initial r.m.s. Mach number and the initial values of density variance and χ on the evolution of turbulent shear flow.

The typical development of the turbulence during a simulation is as follows. Initially the shear stress, $\overline{\rho u_1'' u_2''}$, is zero and, hence, there is no production and the turbulence decays. At later times, the shear stress builds up to the point where the production rate outweighs the dissipation rate and the turbulent kinetic energy grows. The integral lengthscales also grow, so that eventually the large eddies fill the computational domain and the simulation must be stopped.

A major problem hindering simulations of compressible turbulence is that the range of lengthscales is broader than for the corresponding incompressible flow. An indication of this is seen by comparing typical incompressible measures of the large and small scales of the turbulence with compressible measures. The large scales of motion are shown by two-point correlations. Figure 6 shows the normalized two-point correlations of the solenoidal velocity and those of the dilatational velocity from scb96 at $St = 14$. The two-point correlations of the solenoidal velocity fall off well within half
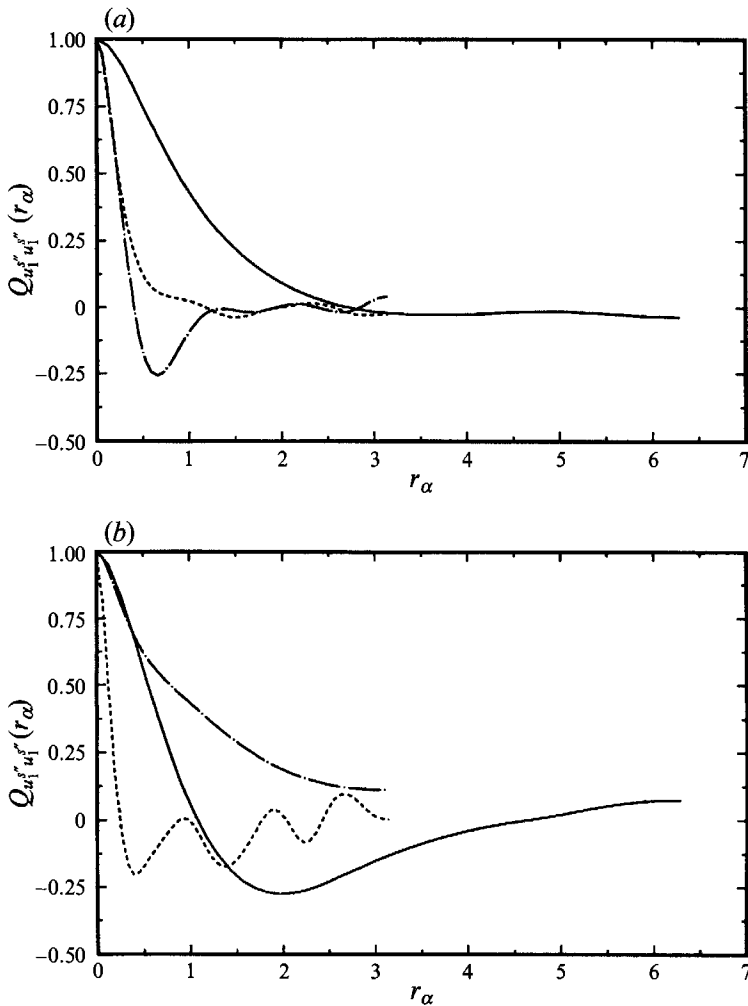
FIGURE 6. (*a*) 2-point correlations of the solenoidal velocity in the x_1-direction for scb96 at $St = 14$. ——, $Q_{u_1^{s'} u_1^{s'}}(r_1)$; ——, $Q_{u_1^{s'} u_1^{s'}}(r_2)$; — · —, $Q_{u_1^{s'} u_1^{s'}}(r_3)$. (*b*) 2-point, correlations of the x_2-component of the dilatational velocity for scb96 at $St = 14$. ——, $Q_{u_2^{d'} u_2^{d'}}(r_1)$; ———, $Q_{u_2^{d'} u_2^{d'}}(r_2)$; — · —, $Q_{u_2^{d'} u_2^{d'}}(r_3)$.

the length of the computational domain, showing that the large lengthscales associated with the solenoidal velocity field are well captured. The two-point correlations of the dilatational velocity, on the other hand, do not fall off as well and show some influence of the periodic boundary conditions. Therefore, the large lengthscales associated with the compressible part of the flow field are larger than those associated with the incompressible part.

A measure of the small scales is gained from examining the dissipation spectrum. Since the dissipation rate of turbulent kinetic energy can be split into two parts, it is useful to consider two separate dissipation spectra. The solenoidal dissipation rate is proportional to the enstrophy and so is described by the enstrophy spectrum,

$$E_{\omega\omega}(k) = \iint \hat{\omega}_i' \hat{\omega}_i'^{\dagger} \, dA(k), \qquad (4.16)$$

where integration is over spherical shells and $\dagger$ denotes a complex conjugate. The
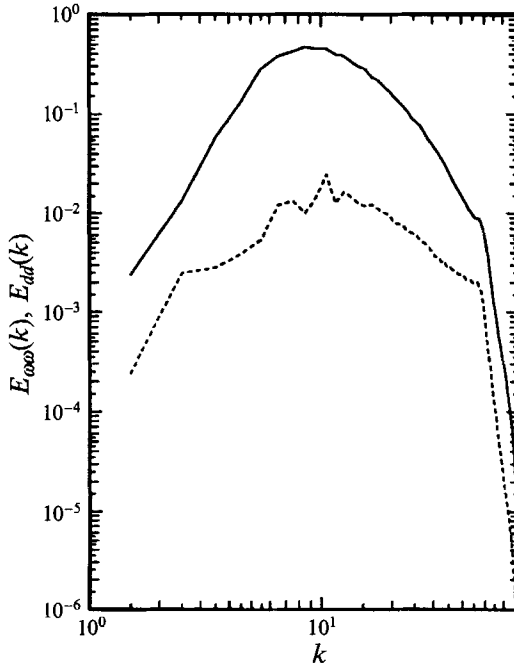
FIGURE 7. Enstrophy spectrum, ———, $E_{\omega\omega}(k)$ and dilatation spectrum, -----, $E_{dd}(k)$
for scb96 at $St = 10$.

dilatational dissipation rate is proportional to the mean squared fluctuating dilatation and is therefore associated with the dilatation spectrum,

$$E_{d'd'}(k) = \iint \hat{d}'\hat{d}'^{\dagger}\,\mathrm{d}A(\boldsymbol{k}). \tag{4.17}$$

Figure 7 shows the enstrophy spectrum and the dilatation spectrum for case scb96 at $St = 10$. The dilatation spectrum does not decay as quickly at high wavenumbers as the enstrophy spectrum. Therefore, the dilatation is more difficult to resolve than the enstrophy, making simulations of compressible turbulence more difficult than those of incompressible turbulence.

We have seen that the range of lengthscales using typical incompressible measures is not as broad as that using compressible measures. Therefore, it seems that compressible turbulence has a broader range of lengthscales for a given Reynolds number. This means that a compressible simulation must either use more grid points than a corresponding incompressible simulation or be limited to lower Reynolds numbers.

Incompressible homogeneous shear flow is determined by two parameters, the shear rate, $S^{\star} = \bar{\rho}^{\star}S^{\star}q^{\star 2}/\epsilon^{\star}$, and the turbulent Reynolds number, $Re_T = \bar{\rho}^{\star 2}q^{\star 4}/\epsilon^{\star}\bar{\mu}^{\star}$. The current simulations are compared with the incompressible simulations of Rogers *et al.* (1986), and so we need to compare the evolution of $S^{\star}$ and Re_T. For both the incompressible and compressible simulations, $S^{\star}$ initially decays to a value near 3 and then grows. The evolution of $S^{\star}$ for the compressible simulations follows closely that of the two incompressible simulations C128V and C128W of Rogers *et al.* The results for C128W increase to about 14 and then drop toward a lower, possibly asymptotic value. The values for C128V rise to 16. They do not decrease, but it is believed that
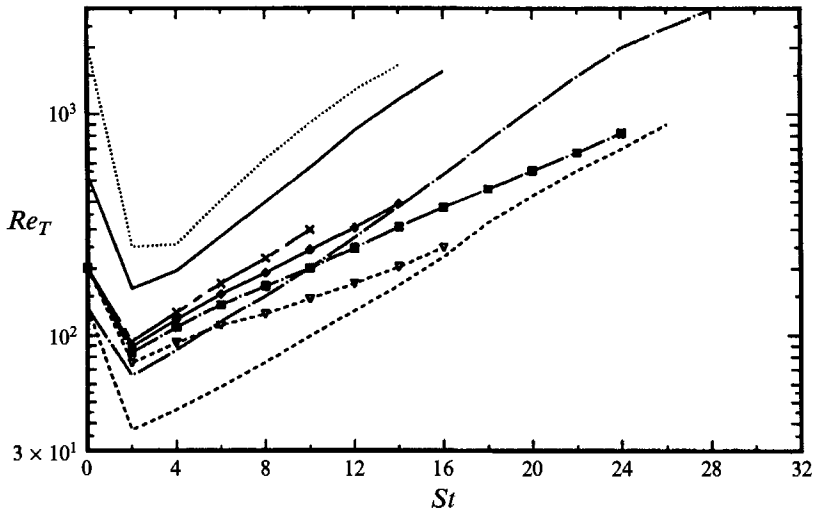
FIGURE 8. History of the turbulent Reynolds number, Re_T, for the incompressible simulations of Rogers, ———, C128U; ————, C128V; — $\cdot$ —, C128W; $\cdots$, C128X; and the compressible simulations ×, sia96; ◆, scb96; ⊠, sha192; ▽, sea96.

they would do so if the simulation could be taken further in time. A large value of $S^\star$ is the assumption made in rapid distortion theory (RDT; see Hunt & Carruthers 1990; Lee & Reynolds 1985). Thus simulation C128V would be expected to be the closest of the incompressible simulations to the RDT limit. Simulation sha192 extends the furthest in time of the compressible simulations. It reaches a value of $S^\star$ of 14, but does not show any sign of decreasing at later times.

The evolution of the turbulent Reynolds number for four of the incompressible simulations is shown in figure 8. Simulation C128V has the lowest Reynolds numbers of the four. Re_T for a representative sample of the compressible simulations is also presented in figure 8. The values of the turbulent Reynolds number for the compressible simulations are close to those from the incompressible simulations C128V and C128W. Examining simulation sha192 the values of Re_T are initially close to those of C128W but then tend toward those of C128V.

We have seen that, for the value of $S^\star$ and Re_T used in the compressible simulations, the evolution of these quantities lie between those of the incompressible simulations C128W and C128V of Rogers *et al.* In examining the effects due to compressibility we will make comparisons with these two incompressible simulations.

4.3. *Dependence on initial conditions*

In this section we examine the dependence on initial conditions of compressibility effects for homogeneous shear flow. Figure 9 shows the evolution of χ_ϵ for the shear flow simulations with an initial r.m.s. Mach number of 0.5. The simulations go through a transient phase in which χ_ϵ varies depending on the initial conditions. However, after some development time, χ_ϵ settles down and becomes independent of its initial value. Other measures of compressibility such as χ and the density variance show a similar behaviour. This independence from the initial conditions means that algebraic turbulence models, such as those of Sarkar *et al.* and Zeman, may be able to capture compressibility effects within compressible shear flow.

As with the isotropic simulations, the linear analysis is useful in understanding these results. In §4.1 it was shown that for the linear problem the vorticity and the dilatation
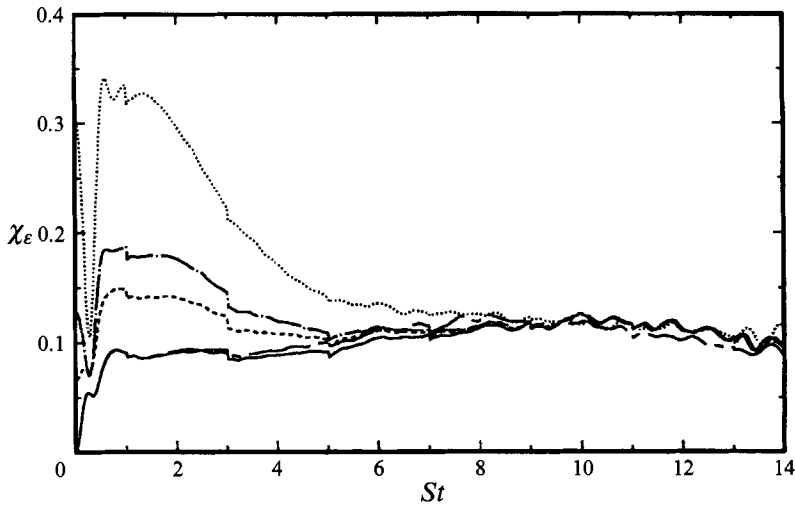
FIGURE 9. Development of χ_ϵ for simulations ——, sea96; — — —, sed96; — · —, see96; · · ·, sef128; — — — —, seg96; which have $M_0 = 0.5$.

are coupled through the mean shear. Since the vorticity and dilatation fields are coupled, energy is exchanged between them. One would therefore expect that the development would become independent of how much energy was initially in each of these fields. This is precisely what is observed in the simulations.

Since the initial values of $\overline{\rho'\rho'}$ and χ do not affect the long-term behaviour of the simulations, only the simulations with these parameters set to zero will be examined further. From these simulations the effect of r.m.s. Mach number on the solutions will be evaluated.

4.4. *Growth rate of the turbulent kinetic energy*

In this section we will examine the growth of the turbulence and determine the effect of r.m.s. Mach number on the growth rate. First, consider the growth of the turbulent Reynolds number, Re_T. The evolution of Re_T for the incompressible turbulent shear flow simulations of Rogers *et al.* (1986) is shown in figure 8. After an initial transient, the curves become nearly straight lines on a semi-log St scale, indicating exponential growth. The slopes of the curves are similar for all of the simulations except at early times. This indicates that, over a variety of conditions, there is a single growth rate for incompressible turbulence.

The exponential growth of turbulence in homogeneous shear flow and the existence of a single growth rate for incompressible turbulence are ideas which are not without controversy. Tavoularis (1985) provided an analysis which predicts an exponential growth of the turbulent kinetic energy. The experiments of Tavoularis & Karnik (1989) have some cases in which the turbulent kinetic energy grows exponentially and some for which it seems to asymptote to a constant level. The latter cases do not extend very far in terms of total strain, which may be the reason exponential growth is not observed. However, the cases which do show exponential growth do not display a universal growth rate. Also, recently Bernard & Speziale (1990) have put forward a theory for which the turbulence grows exponentially and then levels off. Current experiments and simulations do not extend far enough in time to test this theory. Even though the behaviour of incompressible homogeneous turbulent shear flow is not settled, the exponential growth exhibited by the simulations of Rogers *et al.* is clear,
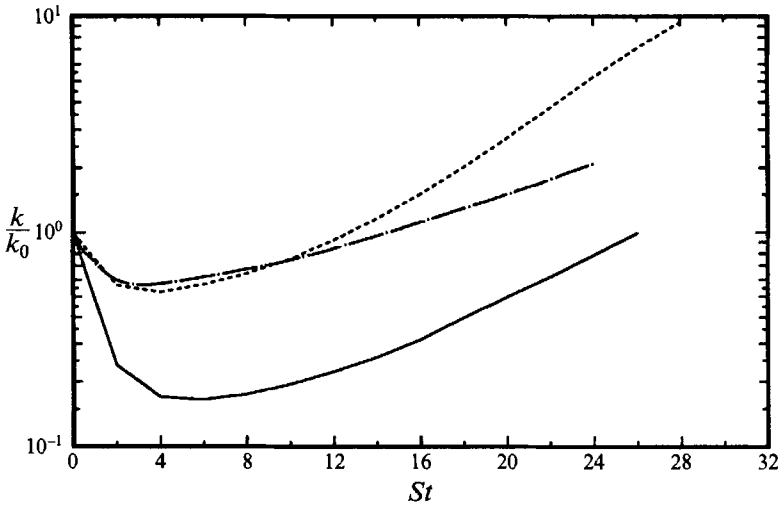
FIGURE 10. Comparison of the normalized turbulent kinetic energy for — · —, sha192 and the incompressible simulations ———, C128V and ----, C128W.

and the results of the compressible simulations will be directly compared to these incompressible simulations.

The compressible simulations shown in figure 8 are sia96, scb96, sha192, and sea96, which have initial r.m.s Mach numbers of 0.2, 0.3, 0.4 and 0.5, respectively. Simulation sia96 has a slope close to that of the incompressible simulations. For the other compressible simulations one sees that as the r.m.s Mach number increases, the growth rate is reduced. The reduction in the growth rate of the turbulence with Mach number is similar to the behaviour that has been observed in experiments and simulations of compressible mixing layers and wakes (Sandham & Reynolds 1991; Chen, Cantwell & Mansour 1990).

In modelling turbulence one is more concerned about the growth rate of the turbulent kinetic energy, k, than the turbulent Reynolds number. However, the turbulent kinetic energy takes longer to develop than Re_T, and the simulations sia96, scb96 and sea96 do not extend far enough in time to see exponential growth in k.

In order to see the development of the turbulence further in time, simulation sha192 was performed using a 192^3 grid. The resolution is the same as for the other simulations, but the computational domain is twice as large in each direction relative to the turbulence lengthscales. This allows the simulation to proceed further in St before the large lengthscales outgrow the computational domain. At $St = 24$ the two-point correlation of the x_2 component of the dilatational velocity begins to show signs of being influenced by the periodic boundary conditions and the simulation is stopped.

The turbulent kinetic energy for sha192 is compared to that of the incompressible simulations C128V and C128W in figure 10. Although there is some variation between the two incompressible simulations, the growth rate of the turbulence for the compressible simulation is clearly reduced. As discussed earlier, the evolution of the non-dimensional shear rate, $S^\star$, and the turbulent Reynolds number, Re_T, shown in figure 8, for the compressible simulation sha192 lie between the values for the incompressible simulations C128V and C128W of Rogers. On this basis the budgets for the turbulent kinetic energy for these simulations can be compared to determine the effects of compressibility.
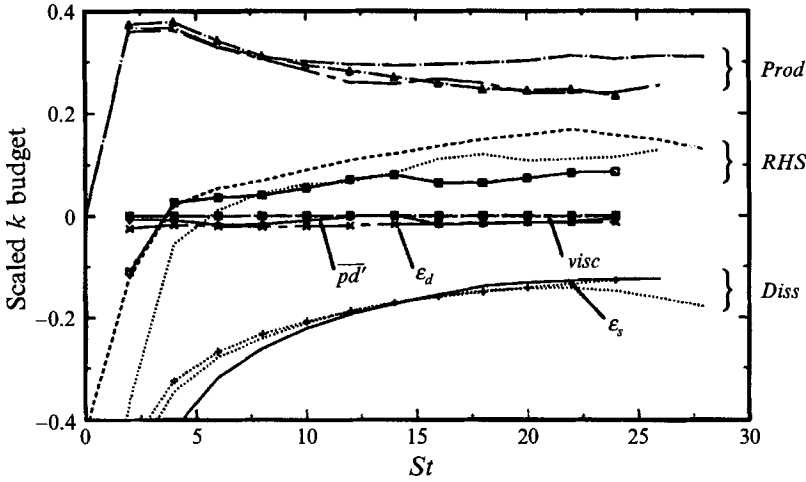
FIGURE 11. Comparison of the scaled turbulent kinetic energy budgets for sha192 and the incompressible simulations C128V and C128W. Simulation sha192 (symbols) extends to $St = 24$, C128V to $St = 26$, and C128W to $St = 28$. *Prod*, production term; *RHS*, right-hand side; *Diss*, dissipation term; *visc*, variable viscosity term.

The turbulent kinetic energy (TKE) equation is examined in order to determine which terms are responsible for the reduced growth rate. When the turbulent kinetic energy equation is scaled by the shear rate and k, the resulting equation is

$$\frac{1}{\overline{\rho u_j'' u_j''}} \frac{d}{d(St)} \overline{\rho u_i'' u_i''} = \frac{2}{\overline{\rho u_j'' u_j''} S} \left\{ \underbrace{-\overline{\rho u_1'' u_2''} S}_{\text{production}} - \underbrace{\frac{\tilde{\mu}}{Re} \overline{\omega_i' \omega_i'}}_{\epsilon_s} - \underbrace{\frac{4}{3} \frac{\tilde{\mu}}{Re} \overline{\left(\frac{\partial u_k''}{\partial x_k} \frac{\partial u_i''}{\partial x_i}\right)}}_{\epsilon_d} + \underbrace{\overline{p' \frac{\partial u_i''}{\partial x_i}}}_{P\text{-dilatation}} \right.$$

$$\left. \underbrace{-\frac{1}{Re} \overline{\mu'' \left(\frac{\partial u_i''}{\partial x_k}\left(\frac{\partial u_i''}{\partial x_k} + \frac{\partial u_k''}{\partial x_i} - \frac{2}{3}\frac{\partial u_l''}{\partial x_l}\delta_{ik}\right)\right)}}_{\text{negligible}} - \underbrace{\frac{S}{Re} \overline{\mu''\left(\frac{\partial u_1''}{\partial x_2}+\frac{\partial u_2''}{\partial x_1}\right)}}_{\text{negligible}} \right\}. \quad (4.18)$$

The reason for using this scaling is that a constant right-hand side in equation (4.18) indicates exponential growth. The first term on the right-hand side is the production term. The second is the solenoidal dissipation rate, ϵ_s, which is the same as the dissipation rate in incompressible turbulence. For incompressible flow, only the first two terms on the right-hand side are present. The third term, ϵ_d, is the dilatational dissipation rate. It is proportional to the mean squared fluctuating dilatation (divergence of velocity) and only occurs in compressible flows. The fourth term is the pressure–dilatation correlation. This term is responsible for the exchange of kinetic and internal energy through the reversible work mode. The last two terms on the right-hand side are correlations involving fluctuations of viscosity (which is temperature dependent); the simulations show that these two terms are negligible.

The scaled TKE equation for sha192 is compared to that for the incompressible simulations in figure 11. The right-hand side of the scaled TKE equation for each of the three simulations does reach an approximately constant value, implying exponential growth. The growth rate for C128V is less than that for C128W mainly because of a smaller production term. The right-hand side for the compressible simulation is

reduced compared to both of the incompressible simulations. We are now in a position to determine which of the terms in the scaled TKE equation are responsible for the reduced growth rate of the compressible simulation.

The production term for sha192 is close to that for C128V, which is less than that for C128W. The reason for the difference in the results for the two incompressible simulations is the low Reynolds number of simulation C128V. Because of the difference in the incompressible simulation results, one cannot tell whether the production term for sha192 is reduced because of compressibility effects or because of low-Reynolds-number effects. In order to make a definite statement about compressibility effects on the production term, compressible simulations at higher Reynolds numbers are needed.

The solenoidal dissipation term has similar values to the dissipation term from the incompressible simulations. This result confirms the modelling assumptions of Sarkar *et al.* (1991 *c*) and Zeman (1990) that the solenoidal dissipation rate can be modelled in the same way as the dissipation rate in incompressible flows. The main reason the right-hand side is reduced for the compressible simulation is the presence of the additional terms in the TKE equation. The dilatational dissipation rate is about 10% of the solenoidal dissipation rate and is an even more significant fraction of the right-hand side. The second compressible term in the TKE balance is the pressure–dilatation term. It oscillates considerably but is roughly of the same magnitude as the dilatational dissipation rate and also acts to reduce the right-hand side. The two terms involving correlations of fluctuating viscosity are essentially zero and can be neglected. Thus, we see that it is both the dilatational dissipation rate and the pressure–dilatation correlation which act to reduce the growth rate of the turbulence in compressible homogeneous shear flow. Models for these terms are examined in the next two sections.

4.5. *Dilatational dissipation*

In §3.3 we mentioned that models for the dilatational dissipation have been proposed by Sarkar *et al.* (1991 *c*) and Zeman (1990) in terms of ϵ_d/ϵ_s. The assumptions made by Sarkar *et al.* and Zeman are quite different. Sarkar's model is based on ideas from linear acoustics while Zeman's model assumes the existence of shock-like structures in the flow. Both models use the turbulent Mach number, M_T, as a parameter. Sarkar's model is

$$\epsilon_d/\epsilon_s = c_S M_T^2, \qquad (4.19)$$

where $c_S = 1.0$, and Zeman's model is of the form

$$\epsilon_d/\epsilon_s = c_Z F(M_T), \qquad (4.20)$$

where in the comparison discussed below the model constant $c_Z = 0.5$. The function $F(M_T)$ is an integral involving the probability density function (PDF) of the Mach number fluctuations. The form given in equation (5) of Zeman (1991) is used for comparison.

Figure 12 shows ϵ_d/ϵ_s plotted as a function of r.m.s. Mach number on log–log axes for the shear flow simulations. The simulations with a given initial r.m.s. Mach number have different values of ϵ_d/ϵ_s depending on χ_0. As the simulations progress (indicated by the arrows) the values of ϵ_d/ϵ_s come together. The value of ϵ_d/ϵ_s, after the effect of initial conditions has disappeared, is the value that should be compared to the models. The solid line shows the model of Sarkar *et al.* and the model of Zeman is shown as the dashed curve. Sarkar's model is seen to do an excellent job compared to the simulations, while Zeman's model predicts a much faster increase of ϵ_d/ϵ_s with r.m.s. Mach number. Overall Sarkar's model matches the results of the simulations more closely.
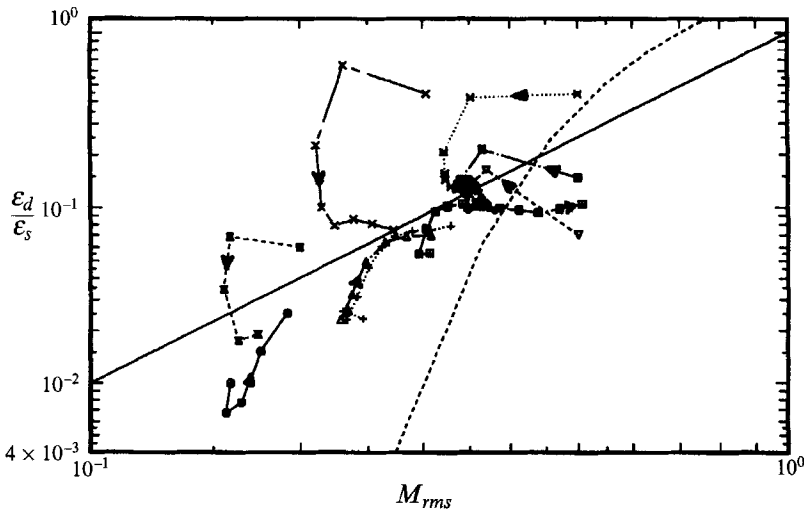
FIGURE 12. Dissipation ratio, ϵ_d/ϵ_s, as a function of M_{rms} for $\oplus$, sia96; $\times$, sic96; $\triangle$, scb96; $+$, scc96; $\times$, scd96; $\diamond$, sea96; ∇, sed96; $\boxtimes$, see96; $\ast$, sef128; $\oplus$, seg96; $\boxplus$, sha192; and for the models of ——, Sarkar $et\ al.$; and ————, Zeman.

Closer examination of the simulation results shows that, beyond $M_{rms} \simeq 0.3$, ϵ_d/ϵ_s flattens out and becomes nearly constant with a value of 0.09. This result is somewhat surprising and we considered several possible reasons for its occurrence. There is a plausible physical explanation for ϵ_d/ϵ_s becoming constant. As the r.m.s. Mach number increases, the dissipation rate increases due to local compression regions (i.e. shock waves). The turbulence may reach the point where the increased dissipation rate is sufficient to keep the r.m.s. Mach number from growing. If there is a limiting value of the r.m.s. Mach number then there would be corresponding limiting values of the measures of compressibility such as ϵ_d/ϵ_s. A limiting r.m.s. Mach number has been predicted in the modelling of a compressible mixing layer by Zeman (1990) and Sarkar & Lakshmanan (1991). Part of the reason case sha192 was run was to test whether there is a limiting r.m.s. Mach number. For the sha192 curve in figure 12, ϵ_d/ϵ_s becomes constant but the r.m.s. Mach number continually increases and no sign of a limiting r.m.s. Mach number is seen. So this does not seem to be the reason for the observed behaviour.

An alternate reason for the levelling off of ϵ_d/ϵ_s is that it may be due to numerical errors. Simulations scb96, scc96 and scd96 outgrow the computational domain at about the same time that ϵ_d/ϵ_s becomes constant so that the issue of box size becomes a concern. Simulation sha192 has a larger computational domain and still has the same behaviour. Therefore, the behaviour is not due to the simulation running out of box size.

Another explanation for the observed behaviour of ϵ_d/ϵ_s becoming constant could be a lack of resolution. The dissipation occurs at small scales and as the r.m.s. Mach number increases it is more likely that shocks will form which will be difficult to resolve. In §5.3 the structure of the turbulence is examined and shocks are found. These shock waves are not well resolved, giving rise to a concern over resolution.

It is not feasible for us to increase the resolution of simulation sha192; however, the effect of resolution can be tested on the 96^3 simulations that exhibit the same behaviour. The fields from scb96 at $St = 10$ were interpolated onto a 192^3 refined mesh and the simulation run to $St = 12$. This new simulation is called scb192. The results of
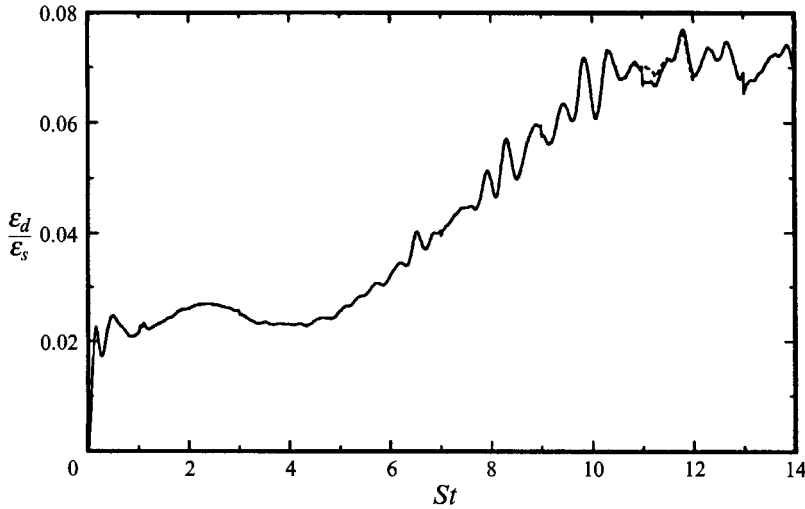
FIGURE 13. Comparison of ϵ_d/ϵ_s for ——, scb96 and ----, scb192 (St = 10–12).

the two simulations are compared in figure 13. The two simulations are nearly identical up to the point of the next remeshing. This is seen as a discontinuity in ϵ_d/ϵ_s for scb96 at $St = 11$. Since simulation scb192 has a refined grid, the remeshing process does not affect the simulation as much. As the simulations evolve after the remesh, the agreement improves. It seems that the effect of the remesh is lost. Overall the agreement of the two simulations is good and ϵ_d/ϵ_s becomes roughly constant for scb192 also. This seems to show that the observed behaviour is not due to a lack of resolution of the small scales. Currently, the reason for the observed behaviour is not known. However, we remain cautious in accepting this result, because even the 192^3 mesh is inadequate for full resolution of the strongest shock waves present in the simulations.

4.6. *Pressure–dilatation correlation*

The second term which is important for modelling of compressible turbulent flows is the pressure–dilatation correlation, $\overline{p\partial u_i''/\partial x_i}$. For decaying isotropic turbulence the pressure–dilation term becomes small after an initial transient. For homogeneous shear flow the pressure–dilatation cannot be neglected.

Zeman (1991) has proposed a model for $\overline{p\partial u_i''/\partial x_i}$. The model relates the pressure–dilatation to the time derivative of the pressure variance by

$$\overline{p\frac{\partial u_i''}{\partial x_i}} = -\frac{1}{2\gamma\bar{p}}\frac{\mathrm{d}}{\mathrm{d}t}\overline{p'p'}. \tag{4.21}$$

The pressure variance is assumed to relax to an equilibrium value, p_e^2, following

$$\frac{\mathrm{d}}{\mathrm{d}t}\overline{p'p'} = -\frac{\overline{p'p'}-p_e^2}{\tau_a}, \tag{4.22}$$

where τ_a is an acoustic timescale. The equilibrium value of the pressure variance is assumed to scale with Mach number as

$$\frac{p_e^2}{\bar{p}^2} = \gamma^2 M_T^2\left(\frac{\alpha M_T^2+\beta M_T^4}{1+\alpha M_T^2+\beta M_T^4}\right), \tag{4.23}$$

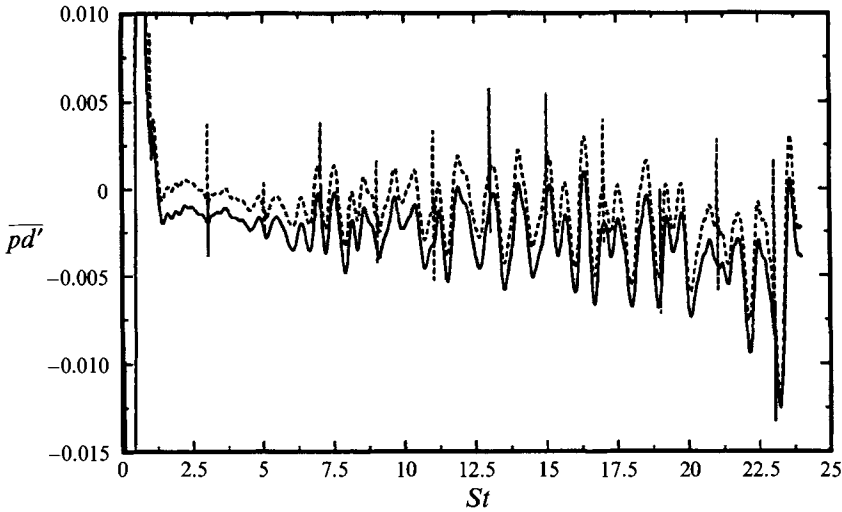FIGURE 14. Test of Zeman's modelling assumption linking ——, the pressure–dilatation, and ———, the time derivative of the pressure variance, using data from sha192.
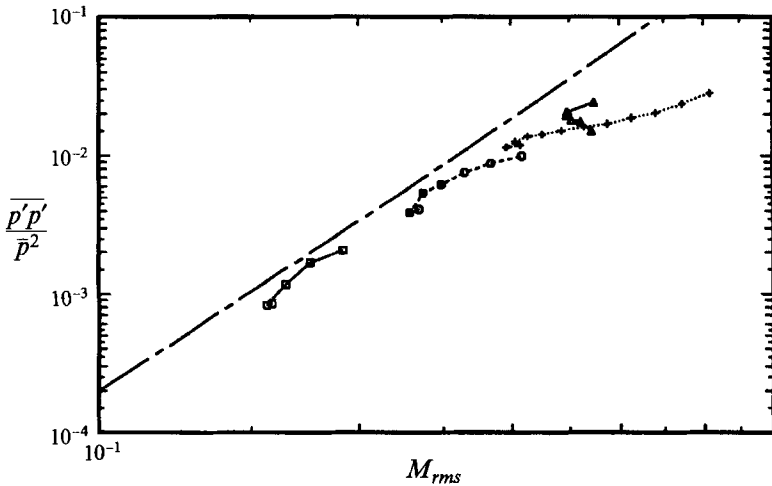

FIGURE 15. Development of the pressure variance scaled by the square of the mean pressure vs. M_{rms} for □, sia96; ○, scb96; △, sea96; +, sha192 and ———, the model of Zeman.

where the reported model constants are $\alpha = 1$ and $\beta = 2$, which were determined by comparison with DNS of decaying isotropic turbulence. This form allows for an M_T^4 behaviour at low r.m.s. Mach numbers, consistent with the acoustic analysis of Sarkar *et al.* (1991 c), and an M_T^2 variation at higher r.m.s. Mach numbers.

Some of the modelling assumptions made by Zeman can be tested directly from the DNS data. Figure 14 compares the pressure–dilatation for case sha192 to the right-hand side (4.21). The agreement is excellent, showing that (4.21) is a good assumption. This is also seen for the isotropic simulations as reported by Zeman (1991). One would not want a turbulence model to follow the detailed oscillations that occur in the simulation. The general trend and order of magnitude of the pressure dilatation can be captured if (4.23) gives the correct scaling. Figure 15 shows the normalized pressure variance, $\overline{p'p'}/\bar{p}^2$, from the shear flow simulations compared to that predicted by (4.23).

At lower r.m.s. Mach numbers the model scales with M_{rms} in the same way as the simulation data, although the pressure variance predicted is somewhat higher than that of the simulations. This may occur because the simulations are not in equilibrium and, therefore, lag the equilibrium value of the pressure variance. At higher r.m.s. Mach numbers the simulation data follows an M_T^2 scaling much sooner than that predicted by the model. Therefore, different values of the model constants or a different form of the fitting function in (4.23) may be needed.

5. Structure of compressible turbulent shear flow

In this section we explore the structure of compressible homogeneous turbulent shear flow. This information provides physical insight and should prove useful for future model development. Probability density functions (PDFs) and flow visualizations are used as tools to gain understanding of the flow. In addition to the velocity and vorticity fields which are studied in incompressible turbulence, we also consider the dilatation and thermodynamic fields which are important for compressible flows. Examination of the compressible aspects of the turbulence reveals the presence of shocks embedded in the flow. This feature is important to our physical understanding of compressible turbulence and to the development of turbulence models for highly compressible flows.

5.1. *Nature of the velocity field*

The velocity field in homogeneous turbulence is essentially Gaussian in that the skewness and flatness are near the values for a Gaussian random process (0 and 3, respectively). However, the velocity derivatives are highly non-Gaussian. The flatness of the velocity derivatives is a measure of the intermittency of the small scales of the turbulence. As in the incompressible case, the intermittency of the small scales increases as the Reynolds number increases.

Compressibility effects on the small scales of the velocity field can best be seen by examining the vorticity and dilatation instead of individual velocity derivatives. The skewness and flatness factors for the vorticity components are given in figure 16 for simulation sha192. Only the x_3 component of the vorticity has a non-zero skewness and it also has the largest flatness value, reaching a value of 5 at $St = 24$. The skewness of the divergence of velocity grows monotonically, similar to that of ω_3, and reaches a value of -1.5 at $St = 24$. The skewness is negative indicating that the strongest dilatations tend to be compressions rather than expansions. The flatness of the dilatation increases to 10 at $St = 24$, which is much greater than the Gaussian value of 3. Comparing these statistics for the vorticity and the dilatation, we find that the dilatation is more highly skewed and more intermittent than the vorticity. This general trend has also been seen by Sarkar (1991*a*).

The skewness and flatness of the dilatation show that there are likely to be strong compression regions or shock waves within the flow. An indication of how much of the flow field contains strong compression regions is given by examining the PDF of the dilatation, $\mathscr{P}_{d'}(d')$. This is shown in figure 17 for simulation sha192 at $St = 24$. By integrating the PDF one can find out how much of the flow has a dilatation more negative than a certain number (negative dilatation indicating compression). However, picking a specific value of the dilatation which represents a 'strong compression' is at best arbitrary.

A better question to address is this: which values of the dilatation, corresponding to compressions, contribute the most to the dilatational dissipation rate and how much of the flow field contains such compressions? Since the dilatational dissipation rate is
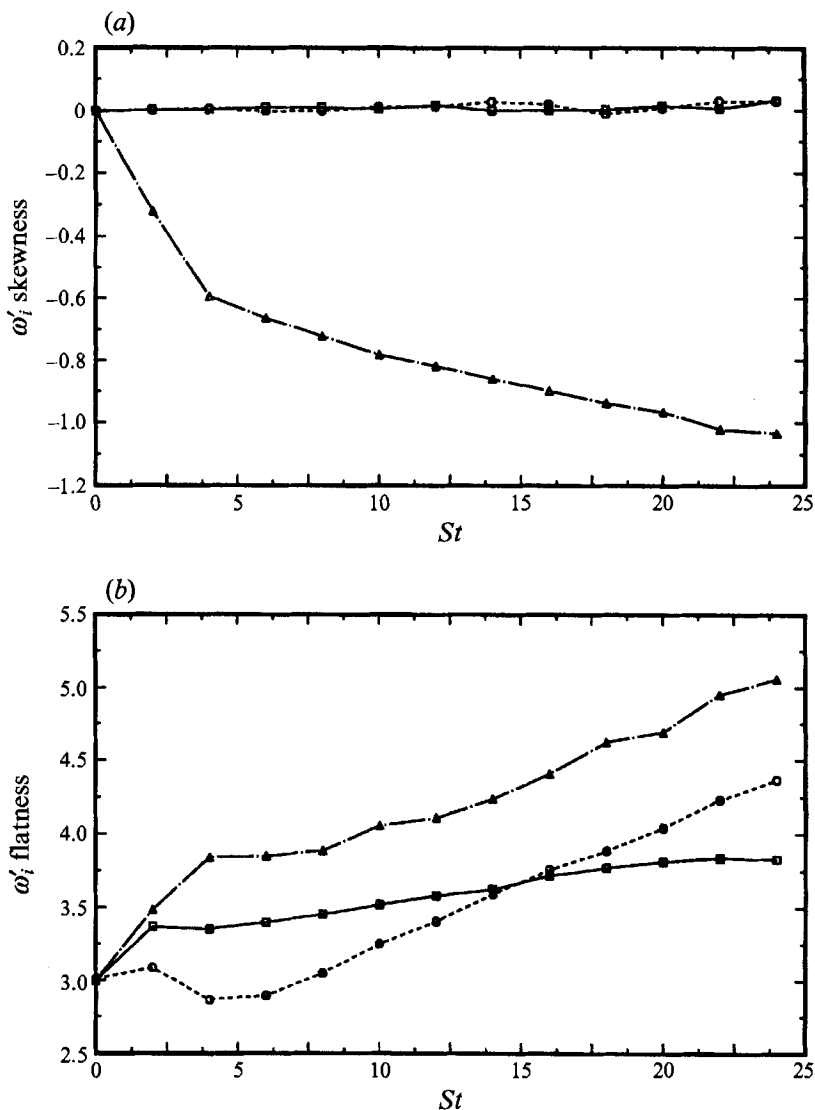
FIGURE 16. Development of (a) the skewness and (b) the flatness of the components of the vorticity for sha192. $\square$, ω_1; $\bigcirc$, ω_2; $\triangle$, ω_3.

proportional to the mean-squared fluctuating dilatation, the answer can be found by examining the weighted PDF

$$\mathscr{P}_{d'}^{w}(d') = \frac{d'^2 \mathscr{P}_{d'}(d')}{\displaystyle\int_{-\infty}^{\infty} d'^2 \mathscr{P}_{d'}(d')\, dd'} \tag{5.1}$$

where $\mathscr{P}_{d'}(d')$, is the PDF of the dilatation. This is plotted in figure 18 for simulation sha192 at $St = 24$. Examining the weighted PDF, $\mathscr{P}_{d'}^{w}(d')$, we see that most of the dilatational dissipation is due to negative dilatations, or compressions, but that a significant amount of the dissipation also comes from low-level positive dilatation. This is also seen for the high-resolution simulation scb192 and is, therefore, not caused
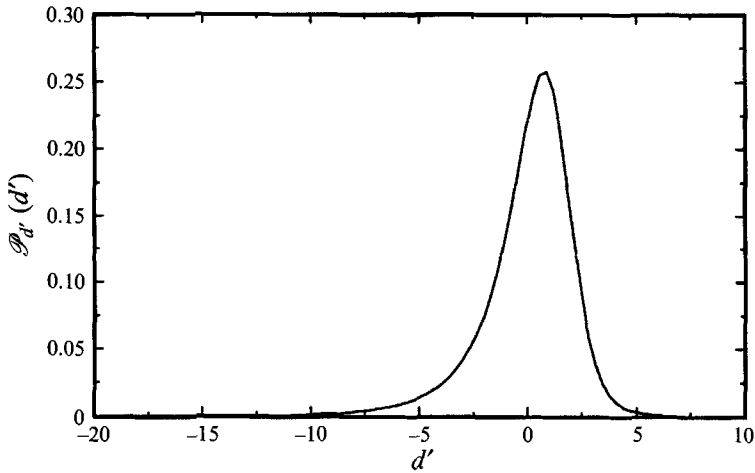
FIGURE 17. PDF of the dilatation for sha192 at $St = 24$.
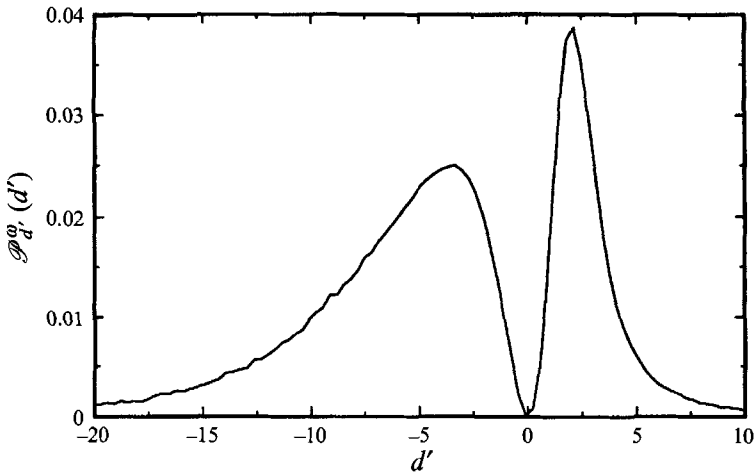
FIGURE 18. Weighted PDF of the dilatation, which gives the contribution to the dilatational dissipation rate, for sha192 at $St = 24$.

by poor resolution. The most extreme values of the dilatation occur infrequently and, therefore, have negligible contributions to the dilatational dissipation, while the moderate values of the dilatation contribute significantly.

The peaks in the weighted PDF show the values of the dilatation that contribute the most to the dissipation rate. From figure 18 we see that peaks for compressive dilatations occurs for $d' = -3.32$. By integrating the PDFs we find that 6.8% of the flow field has a negative dilatation of this magnitude or larger and that these values of the dilatation account for 50.7% of the dilatational dissipation rate. We also find that 23% of the dilatational dissipation rate is due to the most compressive dilatations making up 1% of the flow field while the most compressive dilatations making up 10% of the flow account for 58% of the dilatational dissipation rate. Therefore, moderately strong negative dilatations, which occupy only a small portion of the flow field, contribute significantly to the dilatational dissipation rate, although they are not entirely responsible for the dilatational dissipation.
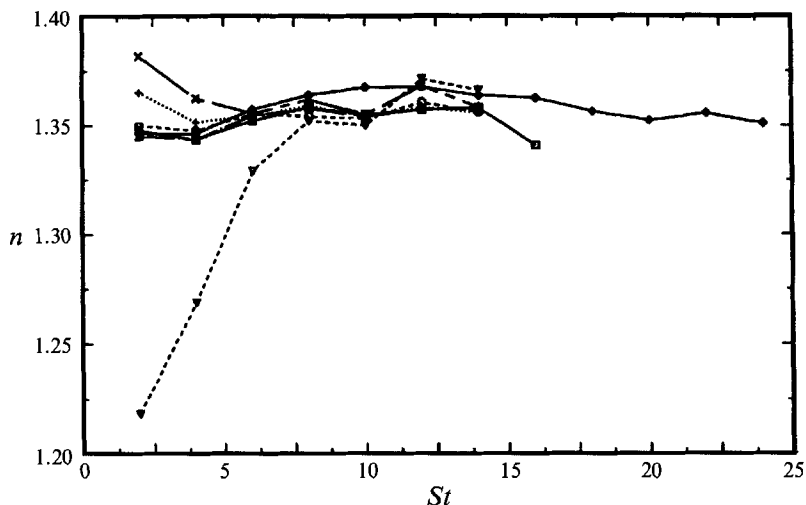
FIGURE 19. Development of the polytropic coefficient for simulations $\square$, sea96; $\bigcirc$, seg96; $\triangle$, sed96; $+$, see96; $\times$, sef128; $\diamond$, sha192; and $\triangledown$, scd96.

The specific values of the dilatation and the percentages cited above are dependent on the level of compressibility in the flow, and we believe are also dependent on the Reynolds number, but the weighted PDF does provide a valuable tool for addressing such questions. The weighted PDF is used further in §5.3. in examining compressible structures.

5.2. Nature of the thermodynamic fields

For compressible turbulence there are fluctuations of the thermodynamic variables, density, temperature and pressure. In turbulence modelling one usually assumes some type of correlation among them. Rubesin (1976) relates these fluctuations through a polytropic coefficient, n,

$$\frac{p'}{\bar{p}} = n\frac{\rho'}{\bar{\rho}} = \frac{n}{n-1}\frac{T''}{\tilde{T}}. \tag{5.2}$$

$n = \gamma$ corresponds to isentropic flow; $n = 1$, isothermal; and $n = 0$, isobaric. The polytropic coefficient is not a well-defined local quantity because it is possible to have $\rho' = 0$ while $p' \neq 0$. One can obtain an 'average' value of n from

$$n = \left(\frac{\overline{p'p'}/\bar{p}^2}{\overline{\rho'\rho'}/\bar{\rho}^2}\right)^{\frac{1}{2}}. \tag{5.3}$$

This average polytropic coefficient is shown for several of the shear flow simulations in figure 19. The value for early times can vary depending on the strength of the entropy fluctuations in the initial conditions. However, the results from all of the simulations tend toward n slightly less than γ ($= 1.4$). Therefore, the density, temperature and pressure fluctuations follow a nearly isentropic process. The results for decaying isotropic turbulence, which are not shown, are more dependent on initial conditions, as would be expected.

The result for shear flow, that the turbulence is nearly isentropic, conflicts with the assumption usually made for compressible boundary layers, that pressure fluctuations are negligible compared to density and temperature fluctuations (Bradshaw 1977). The major reason for this difference is that for a compressible boundary layer there is a density and temperature gradient normal to the wall, while the homogeneous
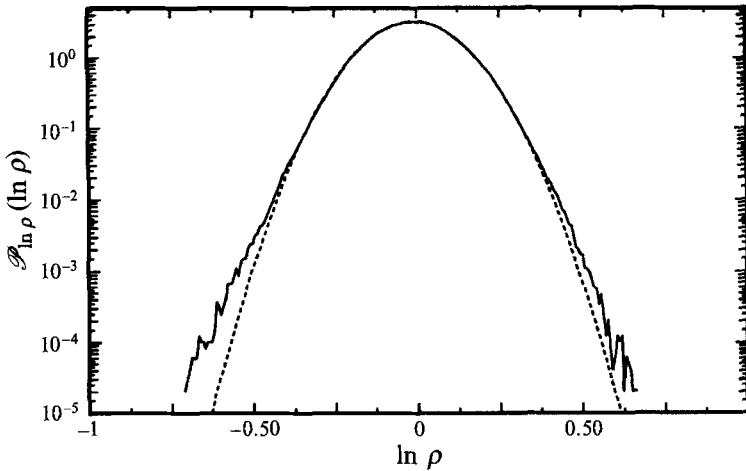
FIGURE 20. ——, PDF of the logarithm of the density, compared to ———, a Gaussian PDF with the same mean and variance, for sha192 at $St = 24$.

simulations do not have a gradient in the mean density or temperature. In a compressible boundary layer the flow is layered and it seems that the turbulence would act to stir up the density and temperature much as it would a passive scalar. This action of the turbulence would give very different behaviour in the fluctuations of density and temperature than is observed in the present homogeneous shear flow simulations.

The nature of the density, pressure and temperature fluctuations can also be seen by considering their individual PDFs. Since the density must be positive, the fluctuations are bounded from below by $\rho' > -\bar{\rho}$. Therefore, it may make sense to consider the PDF of the logarithm of the density, which can be both positive and negative, rather than the density itself. This is shown in figure 20, compared to a Gaussian with the same mean and variance. There is good agreement with the Gaussian except far out in the tails of the PDF. For events near the extrema, the sampling is low, and any lack of resolution in the simulation is likely to show up in this region.

The PDF for the logarithm of the density is nearly Gaussian, which means that the density follows a log–normal distribution. Therefore the probabilities of the density fluctuations are related in a geometric rather than an algebraic fashion. Physically this means that the flow is as likely to undergo a $2:1$ compression as a $1:2$ expansion. The PDFs of the pressure and temperature behave in a similar fashion, although the PDF of $\ln T$ does not agree with the Gaussian as well as that for $\ln \rho$ or $\ln p$. One of the reviewers for this paper noted that there is good reason to expect a log–normal distribution for the density. From the continuity equation in Lagrangian coordinates we have $\rho(t) = \rho(0)\exp\left(-\int \nabla \cdot \boldsymbol{u}\,dt\right)$. If the integration is over a time long compared to the autocorrelation time of the divergence of velocity, then the interval of integration can be broken up to give a sum of independent random variables. From the central limit theorem (Feller 1968), the resulting sum will have a Gaussian distribution, so that the density would be log–normal.

5.3. Compressible turbulent structures

Relatively little is known about structures within a compressible turbulent flow that are directly related to compressibility. Shocks have been observed within decaying isotropic turbulence by several researchers (Passot & Pouquet 1987; Passot *et al.* 1988; Erlebacher 1990; Kida & Orszag 1990*a*; Lee *et al.* 1991). Compressibility effects in
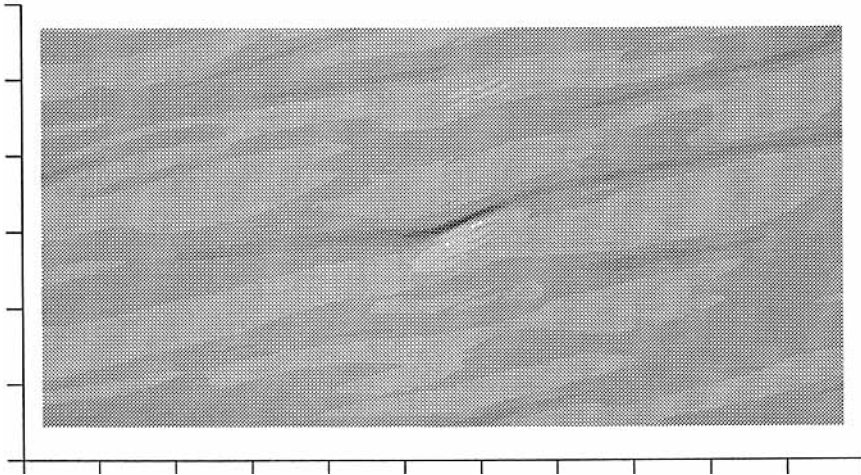
FIGURE 21. Contours of the divergence of the velocity in an (x_1, x_2)-plane for scb192 at $St = 12$. Dark shading corresponds to strong negative dilatation. (The point with the minimum dilatation in the entire field lies in the centre of the plane shown. The view shown is 81×81 grid points.)
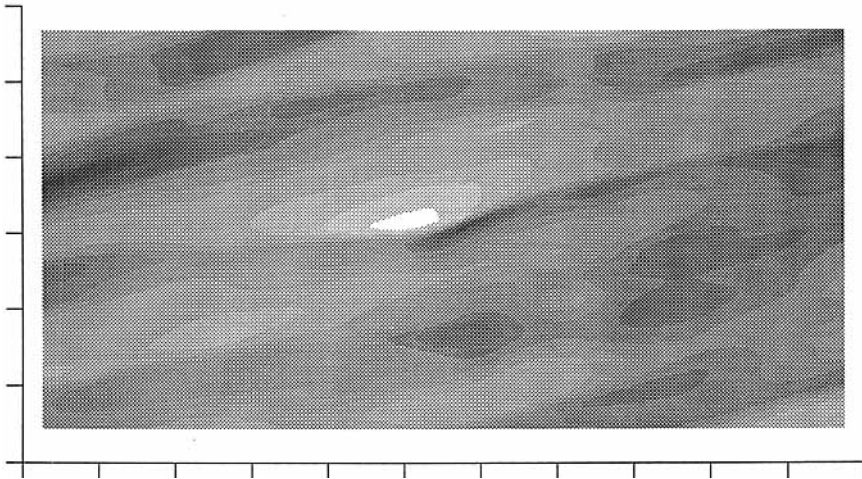

FIGURE 22. Contours of the pressure in the same (x_1, x_2)-plane shown in figure 21. Dark shading corresponds to high pressure.

decaying isotropic turbulence diminish as the turbulence evolves (except at early times when transient effects are strong). However, in compressible shear flow, the turbulence grows in time and compressibility effects become stronger as the flow develops. Since it takes some time for turbulence in a numerical simulation to develop away from its artificial initial conditions, the study of compressible turbulent structures is in some ways easier in homogeneous shear flow than in isotropic turbulence.

First, we examine simulation scb192 at $St = 12$. This simulation is the most highly resolved and gives the most reliable results. We then consider simulation sha192 at $St = 24$. This field has the highest r.m.s. Mach number and the strongest compressibility effects. However, the grid spacing is twice as coarse as for scb192, and the lack of resolution is apparent.

Structures related to the compressibility of the turbulence are expected to be located in regions where the divergence of the velocity is large and negative. Figure 21 shows contours of the divergence of the velocity in an (x_1, x_2)-plane which cuts through the
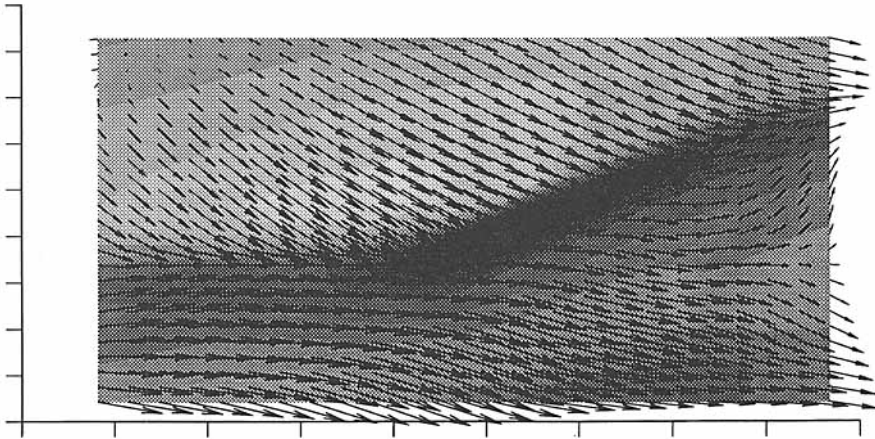
FIGURE 23. Close-up view of contours of pressure with perturbation velocity vectors superposed in the (x_1, x_2)-plane shown in figure 21. (The view shown is 25×25 grid points.)
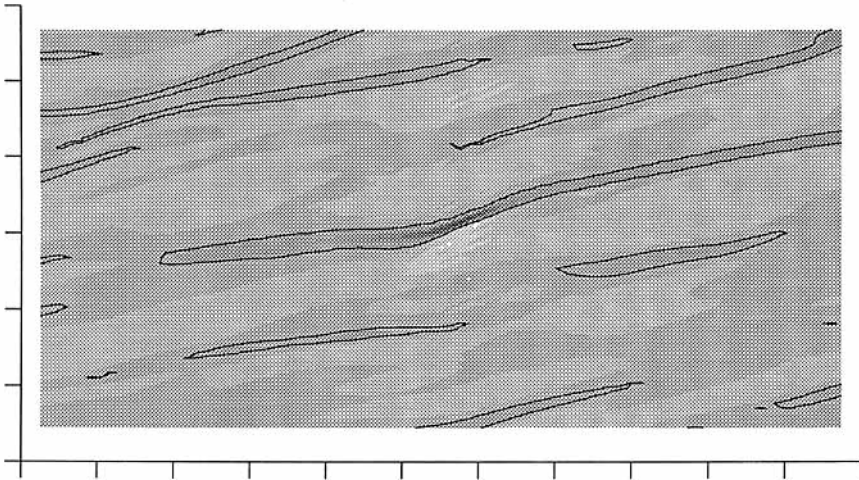

FIGURE 24. Contours of the dilatation in the same plane shown in figure 21 with the contour corresponding to the negative peak in $\mathscr{P}_d^w$ highlighted.

point of strongest dilatation. A thin, elongated region of strong compression lies at an angle of about $20°$ to the x_1-axis. Contours of the pressure in the same plane are shown in figure 22. A similar region of high pressure is present with large gradients where the dilatation is strongest. There is also a large region of low pressure just above the thin region of dilatation. In figure 23 a close-up view of the velocity vectors in the plane are shown. The velocity vectors come down at an angle and suddenly change direction. The compressible structure appears to be an oblique shock wave.

In §5.1 we used the weighted PDF of the dilatation to determine what values of the dilatation were responsible for most of the dilatational dissipation. For simulation scb192 at $St = 12$ the negative peak in $\mathscr{P}_d^w(d')$ occurs at $d' = -0.93$. This value of the dilatation is highlighted in figure 24. The contour is associated with the periphery of the eddy shocklet and weaker compression regions in the area. The values of the dilatation from the strongest part of the shocklet occur too infrequently to contribute significantly to the dilatational dissipation rate. However, since the highlighted contour
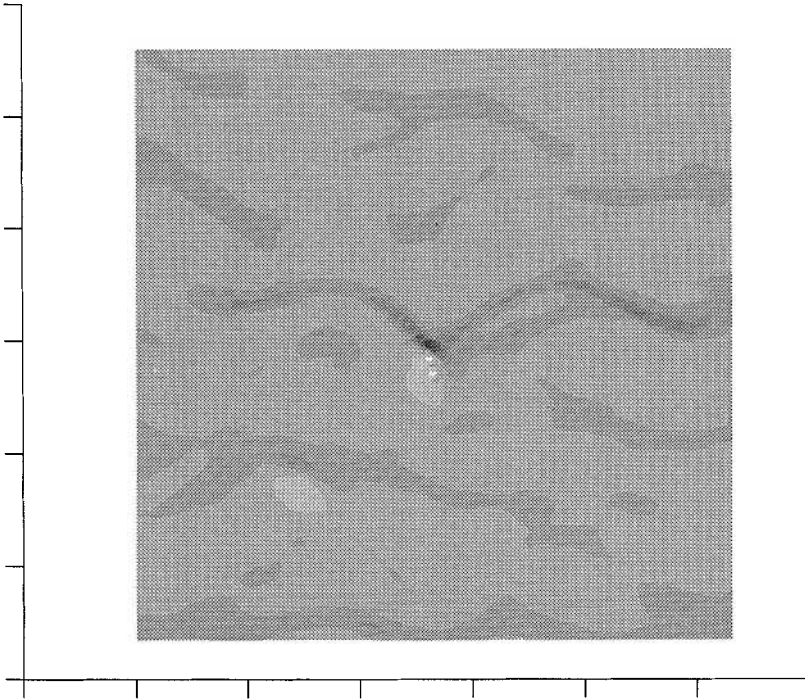
FIGURE 25. Contours of the divergence of the velocity in an (x_2, x_3)-plane which cuts through the point of minimum dilatation in scb192 at $St = 12$. Dark shading corresponds to strong negative dilatation. (The view shown is 81×81 grid points.)

occurs near the eddy shocklet, it appears that eddy shocklets are important to the dynamics of the dilatational dissipation.

The three-dimensional structure of the shock is shown by cutting it with an (x_2, x_3)-plane. Figure 25 shows the dilatation in this plane. The shock wave is thin in the x_2-direction but also does not extend very far in the x_3-direction. The shock is shaped more like a ribbon than the broad sheet that might be expected.

In order to determine how the shocklets arise we consider their relationship to the vortical part of the flow field. The pressure contours presented in figure 22 show that the shock is inclined at an angle of about $20°$ to the direction of the mean velocity. The observed behaviour is suggestive of typical streamwise vortical structures in shear flows. However, as is pointed out below, the vortical structures in the current simulations resemble those seen in rapidly sheared turbulence rather than the hairpin vortices typical of higher-Reynolds-number shear flows.

Figure 26 shows contours of the streamwise vorticity in the spanwise (x_2, x_3)-plane, with velocity vectors overlaid. There is a contour of negative streamwise vorticity and a contour of positive streamwise vorticity which lie on opposite sides of the shock location and which are associated with a downwash just above the shock. The downwash is in the direction of the mean velocity gradient.

From this view, a mechanism for the generation of the shocks seems clear. The vorticity creates a motion in the direction of the mean velocity gradient, either a downwash or an upwash, which causes high-speed and low-speed fluid to come into contact. This causes a compression which results in a shock.

The contours of streamwise vorticity shown in figure 26 suggest the presence of stream-wise vortical structures typical of turbulent shear flows. Figure 27 shows vortex
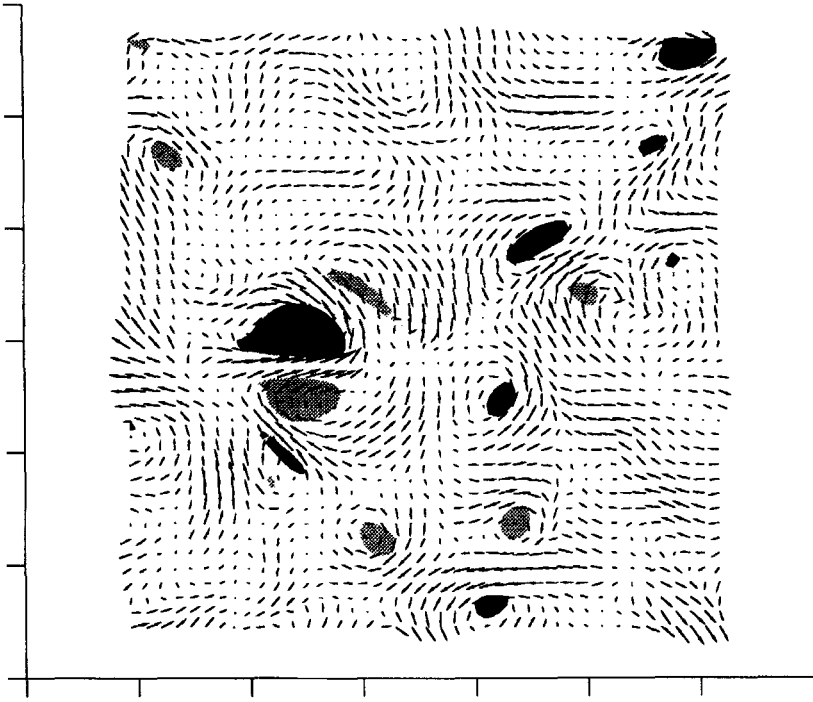
FIGURE 26. Contours of streamwise vorticity with velocity vectors superposed in the same plane shown in figure 25. Dark shading corresponds to negative ω_1, light shading to positive ω_1.
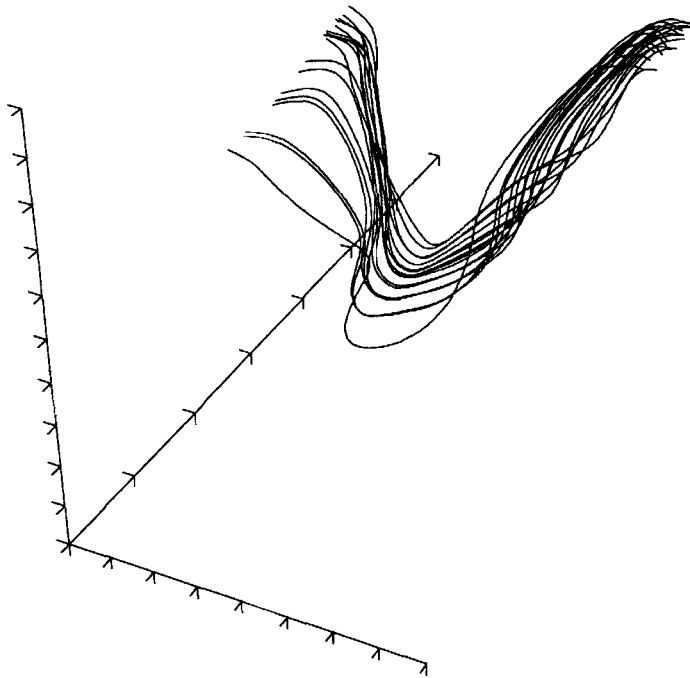

FIGURE 27. Vortex lines which go through the two contours of ω_1 in figure 26 which are associated with the downwash toward the point of minimum dilatation.
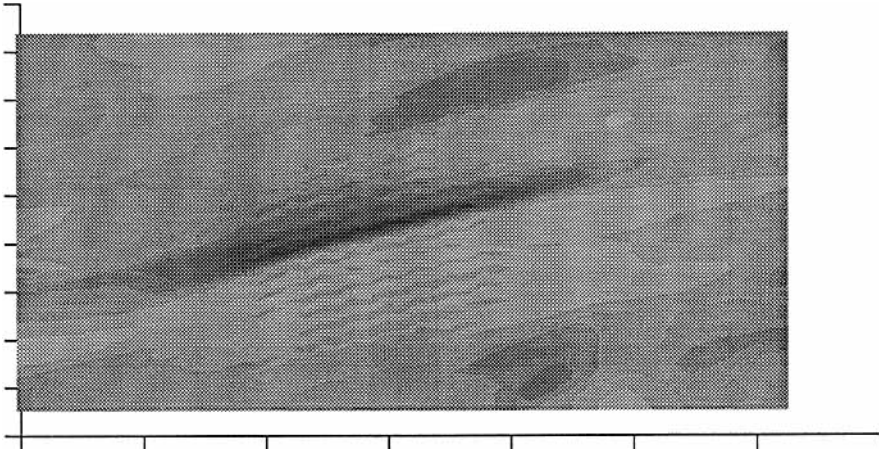
FIGURE 28. Contours of pressure in an (x_1, x_2)-plane for sha192 at $St = 24$. Dark shading corresponds to high pressure. (The point with the minimum dilatation in the entire field lies in the centre of the plane shown. The view shown is 49×49 grid points.)

lines that were started at the centre of the two contours of streamwise vorticity. They form what appears to be an inverted hairpin vortex. The downwash is due to the induced velocity field from these concentrated vortex lines. Further study shows that the vortex lines are part of an irregular corrugated vortex sheet. M. Lee (private communication) has shown that rapidly sheared turbulence results in corrugated vortex sheets, although they are much more regular than those we have observed. Therefore, the current simulations bear some resemblance to rapidly distorted turbulence. Recall that in §4.2 it was pointed out that simulation C128V lay the closest of the incompressible simulations to the rapid distortion limit, and that the parameters for the current simulations are similar to those of this run. The vortical structures of the current simulations are not fully understood, but it appears that streamwise vortices are responsible for the downwash associated with the eddy shocklet.

We next examine the fields from simulation sha192 at $St = 24$. The pressure in an (x_1, x_2)-plane is shown in figure 28. Again, there is a long, thin region of high pressure showing the position of the shock. The structure lies at an angle of 15° to the x_1-axis. There is also a considerable amount of Gibbs' phenomenon, in which strong oscillations occur because the shock is too thin to be resolved on the current grid. This shock is the strongest in the entire flow field and represents the greatest resolution problem. In spite of the lack of resolution, it is believed that the insights gained from this simulation are still useful.

The velocity vectors in the cross-plane $((x_2, x_3)$-plane) are shown in figure 29 superposed on contours of streamwise vorticity. The shock results from a strong upwash associated with a vortex pair. The same mechanism appears responsible for the generation of the shock.

The mechanism discussed above is not the only plausible way shocklets may be created. In order to be certain of the mechanism, the temporal evolution of the eddy shocklet would have to be examined. This would be somewhat difficult since the grid moves in time, but such an investigation should provide valuable information.
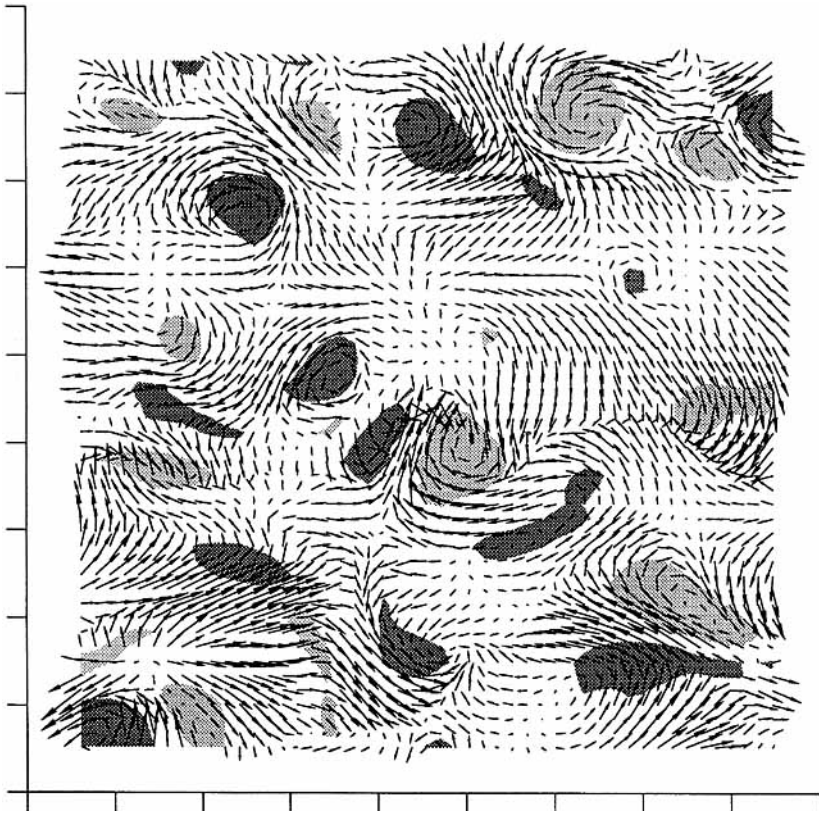
FIGURE 29. Contours of streamwise vorticity with velocity vectors superposed. Dark shading corresponds to negative ω_1, light shading to positive ω_1. (The plane shown is an (x_2, x_3)-plane which cuts through the point of minimum dilatation in sha192 at $St = 24$. The view shown is 49×49 grid points.)

6. Conclusions

Compressible homogeneous turbulence has been studied using direct numerical simulation. Two classes of flows have been considered: decaying isotropic turbulence and homogeneous shear flow. In order to determine the effect of compressibility on the turbulence, the initial r.m.s. Mach number as well as the initial levels of density, temperature and dilatational velocity fluctuations have been varied. Some recently proposed turbulence models for compressible flows have been investigated.

The simulations of decaying isotropic turbulence show that, in the absence of mean deformation, the evolution of compressibility effects, such as the fraction of dissipation rate due to dilatation, χ_e, are dependent on the initial conditions. If the initial conditions do not include any acoustic-type fluctuations, compressibility effects will develop more weakly than if these fluctuations are initially present. This behaviour is consistent with the linear equations with no mean flow, which show that the vorticity mode and the acoustic mode are decoupled. The recently proposed models for compressible flow assume that χ_e is uniquely determined by the r.m.s. Mach number. Since this is not the case for decaying isotropic turbulence, these models cannot work in general for this flow. The dependence on initial conditions also points to the importance of accounting for history effects in flows that have regions of low mean strain.

The simulations of homogeneous shear flow show that the turbulence evolves to become independent of the initial level of acoustic-type fluctuations. This independence from its initial conditions means that simple algebraic turbulence models may be able to correctly capture compressibility effects within shear flows. The observed behaviour can be understood from the linear equations which show that the vorticity and acoustic modes are coupled in the presence of mean shear.

The compressible homogeneous shear flow simulations exhibit a reduction in the growth rate of the turbulence compared to incompressible simulations. The principal reason for this reduction is the dissipation rate due to dilatation, ϵ_d, and the pressure–dilatation correlation. Both of these terms in the turbulent kinetic energy equation occur only for compressible flows.

The evolution of the ratio of the dilatational and solenoidal dissipation rates, ϵ_d/ϵ_s, in the simulations agrees very well with the M_{rms}^2 variation predicted by the model of Sarkar *et al.* (1991 *c*) up to $M_{rms} \simeq 0.3$. For higher r.m.s. Mach numbers ϵ_d/ϵ_s from the simulations becomes roughly constant. While this result could be due to lack of resolution, a test with a refined grid gave identical results which would suggest that the behaviour is not spurious. However, we remain cautious in accepting this result.

Zeman (1991) has proposed a model for the pressure–dilatation correlation in terms of the variance of the pressure. The basic concept of this model has been shown to be valid; however, the variation of $\overline{p'p'}$ with M_{rms} from the simulations is somewhat different at higher r.m.s. Mach numbers from that assumed.

The effect of compressibility on the structure of the turbulence is most noticeable in the formation of eddy shocklets. In shear flow these occur as eddy motions transporting fluid in the direction of the mean velocity gradient. It is believed that they form when low-speed and high-speed fluid elements are brought together. The formation of shock waves causes the simulations to become poorly resolved. The effect of resolution on the results has been addressed and, although the results do not seem to be affected, the issue of resolution remains a concern.

A weighted PDF of the dilatation has been defined which gives the contribution to the dilatational dissipation rate. It shows that intermediate values of the dilatation, which occur on the periphery of the strongest eddy shocklets and throughout weaker compression zones, contribute the most to the dilatational dissipation rate.

The fluctuations of density, pressure and temperature closely follow that of an isentropic process. The presence of shock waves just mentioned would seem to indicate that the turbulence should not behaviour isentropically. However, for weak shocks very little entropy is produced and the observed results are not contradictory. The density, pressure and temperature have probability density functions which agree well with the log–normal distribution.

This study has left many unanswered questions and has raised some new ones that deserve further investigation. In order to determine compressibility effects on the production term in the turbulent kinetic energy equation, simulations at higher Reynolds number are required. The result that ϵ_d/ϵ_s becomes constant at higher r.m.s. Mach numbers needs to be verified. We were unable to ascertain whether a limiting value of the r.m.s. Mach number exists; however, testing of this important concept warrants further simulations. Lastly, the mechanism of eddy shocklet generation should be studied in more detail.

REFERENCES

ARAKAWA, A. 1966 Computational design for long-term numerical integration of the equations of fluid motion: two-dimensional incompressible flow. Part 1. *J. Comput. Phys.* **1**, 119–143.

ARIS, R. 1962 *Vectors, Tensors, and the Basic Equations of Fluid Mechanics.* Prentice–Hall, NJ.

BERNARD, P. S. & SPEZIALE, C. G. 1990 Bounded energy states in homogeneous turbulent shear flow – an alternative view. *ICASE Rep.* 90–66.

BLAISDELL, G. A., MANSOUR, N. N. & REYNOLDS, W. C. 1991*a* Numerical simulation of compressible homogeneous turbulence. *Rep.* TF-50. Department of Mechanical Engineering, Stanford University, Stanford, CA. (Referred to as BMR in the text.)

BLAISDELL, G. A., MANSOUR, N. N. & REYNOLDS, W. C. 1991*b* Compressibility effects on the growth and structure of homogeneous turbulent shear flow. *Proc. Eighth Symp. on Turbulent Shear Flows, Munich, Sept 9–11.*

BRADSHAW, P. 1977 Compressible turbulent shear layers. *Ann. Rev. Fluid Mech.* **9**, 33–54.

CHANDRASEKHAR, S. 1951 The fluctuations of density in isotropic turbulence. *Proc. R. Soc. Lond.* A**210**, 18–25.

CHEN, J. H., CANTWELL, B. J. & MANSOUR, N. N. 1990 The effect of Mach number on the stability of a plane supersonic wake. *Phys. Fluids* A**2** (6), 984–1004.

CHU, B.-T. & KOVASZNAY, L. S. G. 1958 Non-linear interaction in a viscous heat-conducting compressible gas. *J. Fluid Mech.* **3**, 494–514.

DAHLBURG, J. P., DAHLBURG, R. B., GARDNER, J. H. & PICONE, J. M. 1990 Inverse cascade in two-dimensional compressible turbulence. I. Incompressible forcing at low Mach number. *Phys. Fluids* A**2**, 1481–1486.

DANG, K. & MORCHOISNE, Y. F. 1987 Numerical simulation of homogeneous compressible turbulence. *2nd Intl Symp. on Transport Phenomena in Turbulent Flows, Tokyo, Oct. 25–29, 1987.*

DELORME, P. 1985 Simulation numérique de turbulence homogène compressible avec ou sans cisaillement imposé. PhD thesis, University of Poitiers. Available in English as: Numerical simulation of compressible homogeneous turbulence. *European Space Agency Tech. Trans.* ESA-TT-1030, 1988, and *NASA Rep.* N89-15365.

ERLEBACHER, G. 1990 Direct simulation of compressible turbulence. *IMACS First Intl Conf. on Comput. Phys., University of Colorado, Boulder, CO, June 11–15, 1990.*

ERLEBACHER, G., HUSSAINI, M. Y., KREISS, H. O. & SARKAR, S. 1990 The analysis and simulation of compressible turbulence. *Theoret. Comput. Fluid Dyn.* **2**, 73–95.

ERLEBACHER, G., HUSSAINI, M. Y., SPEZIALE, C. G. & ZANG, T. A. 1992 Toward the large-eddy simulations of compressible turbulent flows. *J. Fluid Mech.* **238**, 155–185.

FAVRE, A. 1965*a* Equations des gaz turbulents compressibles. I. *J. Méc.* **4** (3), 361–390.

FAVRE, A. 1965*b* Equations des gaz turbulents compressibles. II. *J. Méc.* **4** (4), 391–421.

FEIEREISEN, W. J., REYNOLDS, W. C. & FERZIGER, J. H. 1981 Numerical simulation of a compressible, homogeneous, turbulent shear flow. *Rep. TF-13.* Department of Mechanical Engineering, Stanford University, Stanford, CA.

FEIEREISEN, W. J., SHIRANI, E., FERZIGER, J. H. & REYNOLDS, W. C. 1982 Direct simulations of homogeneous turbulent shear flows on the Illiac IV computer: applications to compressible and incompressible modelling. *Turbulent Shear Flows 3*, pp. 309–319. Springer.

FELLER, W. 1968 *An Introduction to Probability Theory and Its Applications*, vol. 1, 3rd edn. John Wiley & Sons.

HINZE, J. O. 1975 *Turbulence*, 2nd edn. McGraw-Hill.

HUNT, J. C. R. & CARRUTHERS, D. J. 1990 Rapid distortion theory and the 'problems' of turbulence. *J. Fluid Mech.* **212**, 497–532.

KADOMTSEV, B. B. & PETVIASHVILI, V. I. 1973 Acoustic turbulence. *Sov. Phys. Dokl.* **18** (2) 115–116.

KIDA, S. & ORSZAG, S. A. 1990*a* Enstrophy budget in decaying compressible turbulence. *J. Sci. Comput.* **5** (1), 1–34.

KIDA, S. & ORSZAG, S. A. 1990*b* Energy and spectral dynamics in forced compressible turbulence. *J. Sci. Comput.* **5** (2), 85–125.

KOVASZNAY, L. S. G. 1953 Turbulence in supersonic flow. *J. Aeronaut. Sci.* **20**, 657–682.

KWAK, D., REYNOLDS, W. C. & FERZIGER, J. H. 1975 Three-dimensional, time-dependent computation of turbulent flow. *Rep. TF-5*. Department of Mechanical Engineering, Stanford University, Stanford, CA.

LEE, M. J. & REYNOLDS, W. C. 1985 Numerical experiments on the structure of homogeneous turbulence. *Rep. TF-24*. Department of Mechanical Engineering, Stanford University, Stanford, CA.

LEE, S., LELE, S. K. & MOIN, P. 1991 Eddy-shocklets in decaying compressible turbulence. *Phys. Fluids* A **3**, 657–664.

LIGHTHILL, M. J. 1952 On sound generated aerodynamically. I. General theory. *Proc. R. Soc. Lond.* **211**A, 564–587.

LIGHTHILL, M. J. 1954 On sound generated aerodynamically. II. Turbulence as a source of sound. *Proc. R. Soc. Lond.* **222**A, 1–32.

LIGHTHILL, M. J. 1955 The effect of compressibility on turbulence. *Gas Dynamics of Cosmic Clouds: A Symposium, Cambridge, England, 6–11 July, 1953*.

LIGHTHILL, M. J. 1956 Viscosity effects in sound waves of finite amplitude. *Surveys in Mechanics* (ed. G. K. Batchelor & R. M. Davies). Cambridge University Press.

LIGHTHILL, M. J. 1962 Sound generated aerodynamically. *Proc. R. Soc. Lond.* A **267**, 147–182.

L'VOV, V. S. & MIKHAĬLOV, A. V. 1978*a* Sound and hydrodynamic turbulence in a compressible liquid. *Sov. Phys., J. Exp. Theor. Phys.* **47** (4), April 1978.

L'VOV, V. S. & MIKHAĬLOV, A. V. 1978*b* Scattering and interaction of sound with sound in a turbulent medium. *Sov. Phys., J. Exp. Theor. Phys.* **48** (5), Nov. 1978.

MOISEEV, S. S., SAGDEEV, R. Z., TUR, A. V. & YANOVSKII, V. V. 1977 Structure of acoustic-vortical turbulence. *Sov. Phys. Dokl.* **22** (10), Oct. 1977.

MOISEEV, S. S., PETVIASHVILY, V. I., TOOR, A. V. & YANOVSKY, V. V., 1981 The influence of compressibility on the selfsimilar spectrum of subsonic turbulence. *Physica* **2**D, 218–223.

MONIN, A. S. & YAGLOM, A. M., 1971 *Statistical Fluid Mechanics: Mechanics of Turbulence.* The MIT Press, Cambridge, MA.

MORKOVIN, M. V. 1962 Effects of compressibility on turbulent flows. *Mechanique de la Turbulence,* CNRS, Paris, 1962.

MOYAL, J. E. 1951 The spectra of turbulence in a compressible fluid; eddy turbulence and random noise. *Proc. Camb. Phil. Soc.* **48**, 329–344.

NORMAN, M. L. & WINKLER, K.-H. A. 1985 Supersonic jets. *Los Alamos Sci.* Spring/Summer.

PASSOT, T. & POUQUET, A. 1987 Numerical simulation of compressible homogeneous flows in the turbulent regime. *J. Fluid Mech.* **181**, 441–466.

PASSOT, T., POUQUET, A. & WOODWARD, P., 1988 The plausibility of Kolmogorov-type spectra in molecular clouds. *Astron. Astrophys.* **197**, 228–234.

ROGALLO, R. S. 1981 Numerical experiments in homogeneous turbulence. *NASA Tech. Mem.* 81315.

ROGERS, M. M., MOIN, P. & REYNOLDS, W. C. 1986 The structure and modeling of the hydrodynamic and passive scalar fields in homogeneous turbulent shear flow. *Rep. TF-25*. Department of Mechanical Engineering, Stanford University, Stanford, CA.

RUBESIN, M. W. 1976 A one-equation model of turbulence of use with the compressible Navier–Stokes equations. *NASA Tech. Mem.* X-73, 128.

SANDHAM, N. D. & REYNOLDS, W. C. 1991 Three-dimensional simulations of large eddies in the compressible mixing layer. *J. Fluid Mech.* **224**, 133–158.

SARKAR, S., ERLEBACHER, G. & HUSSAINI, M. Y. 1991*a* Direct simulation of compressible turbulence in a shear flow. *Theoret. Comput. Fluid Dyn.* **2**, 291–305.

SARKAR, S., ERLEBACHER, G. & HUSSAINI, M. Y. 1991*b* Compressible homogeneous shear: simulation and modeling. *Proc. Eighth Symp. Turbulent Shear Flows, Munich, September 9–11.*

SARKAR, S., ERLEBACHER, G. & HUSSAINI, M. Y. 1992 Compressible homogeneous shear: simulation and modeling. *Turbulent Shear Flows 8.* Springer.

SARKAR, S., ERLEBACHER, G., HUSSAINI, M. Y. & KREISS, H. O. 1991*c* The analysis and modelling of dilatational terms in compressible turbulence. *J. Fluid Mech.* **227**, 473–493.

SARKAR, S. & LAKSHMANAN, B. 1991 Application of a Reynolds stress turbulence model to the compressible shear layer., *AIAA J.* **29** (5), 743–749.

STAROSELSKY, I., YAKHOT, V., KIDA, S. & ORSZAG, S. A. 1990 Long-time, large-scale properties of a randomly stirred compressible fluid. *Phys. Rev. Lett.* **65**, 171–174.

TATSUMI, T. & TOKUNAGA, H. 1974 One-dimensional shock turbulence in a compressible fluid. *J. Fluid Mech.* **65** (3), 581–601.

TAVOULARIS, S. 1985 Asymptotic laws for transversely homogeneous turbulent shear flows. *Phys. Fluids* **28** (3), 999–1001.

TAVOULARIS, S. & KARNIK, U. 1989 Further experiments on the evolution of turbulent stresses and scales in uniformly sheared turbulence. *J. Fluid Mech.* **204**, 457–478.

TOKUNAGA, H. & TATSUMI, T. 1975 Interaction of plane nonlinear waves in a compressible fluid and two-dimensional shock turbulence. *J. Phys. Soc. Japan*, **38** (4), 1167–1179.

WHITE, F. M. 1974 *Viscous Fluid Flow.* McGraw-Hill.

WRAY, A. A. 1986 Very low storage time-advancement schemes. *Internal Rep.* NASA Ames Research Center, Moffet Field, CA.

ZAKHAROV, V. E. & SAGDEEV, R. Z. 1970 Spectrum of acoustic turbulence. *Sov. Phys. Dokl.* **15** (4), Nov. 1970.

ZEMAN, O. 1990 Dilatation dissipation: The concept and application in modeling compressible mixing layers. *Phys. Fluids* A**2**, 178–188.

ZEMAN, O. 1991 On the decay of compressible isotropic turbulence. *Phys. Fluids* A**3** (5), 951–955.